

Fourier analysis near-field polarimetry for measurement of local optical properties of thin films

Lori S. Goldner, Michael J. Fasolka, Sophie Nougier, Hoang-Phi Nguyen, Garnett W. Bryant, Jeeseong Hwang, Kenneth D. Weston, Kathryn L. Beers, Augustine Urbas, and Edwin L. Thomas

We present measurements of the local diattenuation and retardance of thin-film specimens by using techniques that combine near-field scanning optical microscopy (NSOM) and a novel polarization-modulation (PM) polarimetry utilizing Fourier analysis of the detected intensity signal. Generally, quantitative near-field polarimetry is hampered by the optical anisotropy of NSOM probes. For example, widely used aluminum-coated pulled-fiber aperture probes typically exhibit a diattenuation near 10%. Our analysis of aperture diattenuation demonstrates that the usual techniques for nulling a PM polarimeter result in a nonzero residual probe retardance in the presence of a diattenuating tip. However, we show that both diattenuation and retardance of the sample can be determined if the corresponding tip properties are explicitly measured and accounted for in the data. In addition, in thin films (<100 nm thick), where the sample retardance and diattenuation are often small, we show how to determine these polarimetric quantities without requiring alignment of the fast and diattenuating axes, which is a more general case than has been previously discussed. We demonstrate our techniques by using two types of polymer-film specimens: ultrahigh molecular weight block copolymers (recently noted for their photonic activity) and isotactic polystyrene spherulites. Finally, we discuss how changes in the tip diattenuation during data collection can limit the accuracy of near-field polarimetry and what steps can be taken to improve these techniques. © 2003 Optical Society of America

OCIS codes: 120.0120, 120.5410, 180.5810, 160.5470.

1. Introduction

Since the introduction of aperture-based near-field scanning optical microscopy (NSOM) more than 15 years ago,^{1,2} it has been the intent of numerous researchers to use this technique to characterize the local optical properties of materials. The need for such a characterization tool is underscored by the

recent emergence of microfabricated and self-assembled photonic devices,³ the efficacy of which depend on the optical properties of submicrometer-length features. To date, however, NSOM studies have been largely qualitative, serving to define the limits of the technique and providing a list of contrast mechanisms governed by, e.g., topography,^{4,5} interference,⁶ and scattering,^{7–11} which, while interesting and often useful, do not entirely meet the goal of measuring local optical properties such as diattenuation and birefringence. Although a large body of literature exists on materials characterized by using NSOM, only a small subset claims to measure material properties quantitatively.

Arguably, of this subset, techniques involving fluorescence measurements, polarization NSOM, or some combination of the two have been most successful in generating quantitative optical data. Simple static polarimetric NSOM (where a specific polarization state of light is used to excite the sample and another polarization state is detected) and the various artifacts that can occur with it have been discussed by many authors^{5,12–14} in many different contexts, including investigations of small metal

When this work was done L. S. Goldner, M. J. Fasolka, S. Nougier, H.-P. Nguyen, G. W. Bryant, J. Hwang, and K. D. Weston were with the Optical Technology Division, National Institute of Standards and Technology, Gaithersburg, Maryland 20899. K. L. Beers is with the Polymers Division, National Institute of Standards and Technology, Gaithersburg, Maryland 20899. M. J. Fasolka is now with the Polymers Division. G. W. Bryant is now with the Atomic Physics Division. K. D. Weston is now with the Department of Chemistry and Biochemistry, Florida State University. A. Urbas and E. L. Thomas are with the Department of Materials Science and Engineering, Massachusetts Institute of Technology, Cambridge, Massachusetts 02139.

Received 5 September 2002; revised manuscript received 13 January 2003.

0003-6935/03/193864-18\$15.00/0

© 2003 Optical Society of America

structures,^{5,12} magnetic films,^{12,15} lipid films,¹⁶ J-aggregates,¹⁷ conjugated polymers,^{18–21} and liquid-crystal droplet structure, dynamics,²² and birefringence.^{22,23} Static polarization techniques have also been used to read, write, and characterize single magnetic bits.²⁴ The introduction of polarization-modulation techniques to NSOM¹³ predicated increases in both the quality and the information content of polarimetric images. For example, Ade *et al.*²⁵ used a modulating analyzer to improve static polarimetry measurements; by modulating the analyzer, one can obtain both parallel- and crossed-polarizer images simultaneously. The authors used this technique to characterize qualitatively the birefringence of Kevlar fibers and polymer-dispersed liquid crystals.²⁵ Polarization modulation (PM) of the excitation light with an electro-optic modulator was used in conjunction with NSOM by Higgins *et al.*²⁶ to measure the orientation of mesoscopic crystals and by the Heinzelmann group to study magnetic and liquid crystalline materials.^{27–29} With corrections for tip diattenuation,³⁰ Tan *et al.*³¹ and Wei *et al.*³² used the same technique to study the diattenuation of thin-film conjugated polymers. A variety of other polarization-modulation (PM) schemes in NSOM can be found,^{33–38} but the above-mentioned schemes constitute those most closely related to this work. The group of J. W. P. Hsu, who presented direct measurements of retardance and fast axis orientation of semiconductor specimens,³⁹ first implemented quantitative NSOM polarimetry capable of both diattenuation and retardance measurements using PM.

In this paper we build on the work of McDaniel *et al.*³⁹ through improved measurement methods and data-analysis techniques that increase the accuracy of retardance and diattenuation measurements and thus provide a better means of characterizing the optical properties of materials structured on the sub-micrometer level. In particular we address challenges that currently denigrate the usefulness and accuracy of polarimetric NSOM (1) by showing how measurements can be made and analyzed on general thin films where the fast and the diattenuating axis need not be the same, (2) by demonstrating the limits of the technique and quantitatively discussing the uncertainties involved, and (3) by showing (for what we believe to be the first time) how to account correctly for tip diattenuation and the resulting residual retardance in PM NSOM data. We demonstrate our NSOM polarimeter on two mesostructured polymer film specimens: (1) ultrahigh molecular weight block copolymers,^{40–42} which microphase separate⁴³ to form domains patterned on an approximately 100-nm length scale and have been recognized recently for their photonic bandgap behavior^{41,42}; and (2) thin-film crystalline polymer spherulites (here of isotactic polystyrene), the understanding of which has benefited significantly from classical far-field polarimetry.⁴⁴

In Section 2 we present a review of the type of PM polarimetry implemented in this work with some simple results derived or quoted and approximations

discussed. In Section 3 we describe the NSOM polarimeter and data acquisition. In Section 4 we show how probe diattenuation and residual retardance can be correctly measured, and in Section 5 we show typical probe-only data and address the problems involved when using an aperture probe. Here the accepted procedure for nulling the retardance of the near-field probe is discussed in terms of uncertainties and errors that can result. In Section 6 we describe the characterization of a generic linearly diattenuating and linearly birefringent sample in the presence of the imperfect tip discussed in Sections 4 and 5. This analysis has fewer assumptions and approximations than in previous work, yet still yields a tractable formalism and allows for the sample diattenuation, diattenuating axis alignment, retardance, and fast axis alignment to be extracted from the data. In Section 7 we present measurements of diattenuation in block copolymer specimens. A discussion of modeling is initiated; preliminary results show that much of the diattenuation contrast observed is due to the unique near-field coupling of the probe and the sample and details of the NSOM aperture. In Section 8 we demonstrate the full power of this technique through the combined retardance and diattenuation measurements of polystyrene spherulites. Finally, in Section 9 we continue the discussion of modeling the tip-sample interaction, consider the applicability of a Jones or Mueller matrix approach to an aperture-confined light source, and discuss other concerns and future possibilities of this technique.

2. Polarization-Modulation Polarimetry

In polarimetry the change in the polarization of light as it passes through a sample is measured and used to ascertain the properties of a material. A typical polarimeter places a sample between a polarization-state generator and a polarization-state analyzer. The polarimetric properties of a homogeneous, stationary material can be described by eight parameters: a global phase change (corresponding to the average index of refraction of a material), a global absorption or transmission, two eigenpolarizations (polarizations for which light propagates through the materials with no polarization state change) specified by four parameters (each has an angle and ellipticity), and the relative phase change and relative absorption (or relative transmittance) for eigenpolarized light (the ratio of the eigenvalues). To completely measure all these parameters, eight independent measurements must be done, varying both the input polarization and the polarization sensitivity of the detector. However, it is often advantageous to apply various approximations and limitations that reduce the number of required measurements. Polarimetric measurements cannot generally be used to determine the overall phase change (due to the average index and thickness) of the material, which would require an interferometric measurement. In this work we do not attempt to measure circular diattenuation or circular retar-

Table 1. Jones Matrices

| $[R(\phi)]$ Rotation through Angle ϕ from the x Axis | $B(\theta)$ Linear Retarder Fast x Axis, Retardance θ | QWR Quarter-Wave Retarder | PEM Retardance Modulation Amplitude d , Frequency ω | $D(u, v)$ Linear Diattenuator, Transmittances u and v | LIN, Linear Polarizer (Perfect) |
|---|---|---|--|---|--|
| $\begin{bmatrix} \cos(\phi) & -\sin(\phi) \\ \sin(\phi) & \cos(\phi) \end{bmatrix}$ | $\begin{bmatrix} \exp\left(-\frac{i\theta}{2}\right) & 0 \\ 0 & \exp\left(\frac{i\theta}{2}\right) \end{bmatrix}$ | $\begin{pmatrix} -i & 0 \\ 0 & 1 \end{pmatrix}$ | $\begin{bmatrix} \exp[-id \sin(\omega t)] & 0 \\ 0 & 1 \end{bmatrix}$ | $\begin{pmatrix} \sqrt{u} & 0 \\ 0 & \sqrt{v} \end{pmatrix}$ | $\begin{pmatrix} 1 & 0 \\ 0 & 0 \end{pmatrix}$ |

Note: Although calculations can be done in either the Mueller or the Jones formalisms (since we do not include depolarization effects), we choose here the Jones formalism for simplicity. Shown above are the Jones matrices used for the calculations contained herein. Equation 1, for example, is the result of a calculation $I = E \cdot E^*$, where

$$E = R(\varphi_d) \times D(q, r) \times B(\theta) \times R^T(\varphi_d) \times R\left(\frac{-\pi}{2}\right) \times \text{QWR} \times R^T\left(\frac{-\pi}{2}\right) \times R\left(\frac{-\pi}{4}\right) \times \text{PEM} \times R^T\left(\frac{-\pi}{4}\right) \times \begin{pmatrix} \sqrt{I_0} \\ 0 \end{pmatrix}.$$

dance of the sample, only linear retardance and linear diattenuation. In addition, other researchers have assumed that the fast and diattenuating axes have identical orientation.^{39,45} Since the assumption of coaligned axes restricts the range of samples that can be examined, it is not employed in this work (except for illustration purposes in this section). Given these assumptions, five parameters are left to be determined: the overall absorption, the relative absorption (dichroism) or transmittance (diattenuation) of the two eigenpolarizations, linear birefringence (or more generally the linear retardance), and orientations of the fast and dichroic or diattenuating axes. Use of a PM technique,^{46,47} described below, further reduces the number of polarizer/analyzer configurations for which data must be acquired. In this work we use only two different configurations of our polarimeter, and Fourier analysis of the detected signal, to obtain these five parameters.

We define the term diattenuation below as the difference in transmittance of two polarization modes of a system. Note that the term dichroism is sometimes used in this capacity, although dichroism more traditionally refers to the difference in absorption coefficients.⁴⁸ Furthermore use of the term dichroism is sometimes constrained to uniaxial crystals rather than systems where scattering or reflection is the main cause of the difference in absorption or transmission.

When the Jones matrix formalism is used, an arbitrary polarization element J can be decomposed into two elements, $J = J_d J_r$, where J_r , a retarder, is represented by a unitary matrix and J_d , a diattenuator, is represented by a non-negative definite Hermitian matrix.⁴⁹ The transmittance of this optical element is given by $T(E) = |JE|^2/|E|^2$ and the diattenuation by⁴⁹

$$\mathcal{D}(J) = \frac{T_{\max} - T_{\min}}{T_{\max} + T_{\min}},$$

where

$$T_{\max} = \max[T(E)] = T(E_{\max}),$$

$$T_{\min} = \min[T(E)] = T(E_{\min}).$$

Here E_{\max} and E_{\min} are the incident fields with maximum and minimum transmittance, T_{\max} and T_{\min} , which can be shown to be the eigenvalues of J_d^2 . Eigenvectors E_{\max} and E_{\min} are orthogonal. For the case of linear diattenuation only, $J = D(u, v)$ is given in Table 1 and the diattenuation reduces to

$$\mathcal{D}[D(u, v)] = \frac{u - v}{u + v},$$

where the transmittances, u and v , are defined such that u is larger. (Note that we define u and v as the transmittances for light polarized parallel and perpendicular to the diattenuating axis; since u is taken to be the larger transmittance, the diattenuating axis therefore represents the polarization direction with the higher transmission.) The definition of retardance is more subtle and involves the difference in the phase of the two eigenpolarizations. Even without specifying the eigenpolarizations for J , we know that since J_r is unitary we can define a phase retardance as⁴⁹

$$\mathfrak{D}(J) = 2 \cos^{-1} \left| \frac{\text{tr } J_r}{2} \right|,$$

which for the case of the linear retarder, $J_r = B(\theta)$ (given in Table 1), gives

$$\mathfrak{D}[B(\theta)] = \theta,$$

as expected. Accordingly the retardance corresponds to the relative phase change between the two eigenpolarizations of J_r as they propagate through the element represented by J . The birefringence of a material, usually defined as the difference in index of refraction in a material for the two eigenpolarizations, can often be calculated from the retardance given some knowledge of sample thickness and alignment.

Note that, while the eigenvectors of both J_r and J_d must be orthogonal, the general matrix J need not have orthogonal eigenpolarizations. If the fast and diattenuating axes are aligned, the eigenvectors of the system (of J) are orthogonal. This case is the

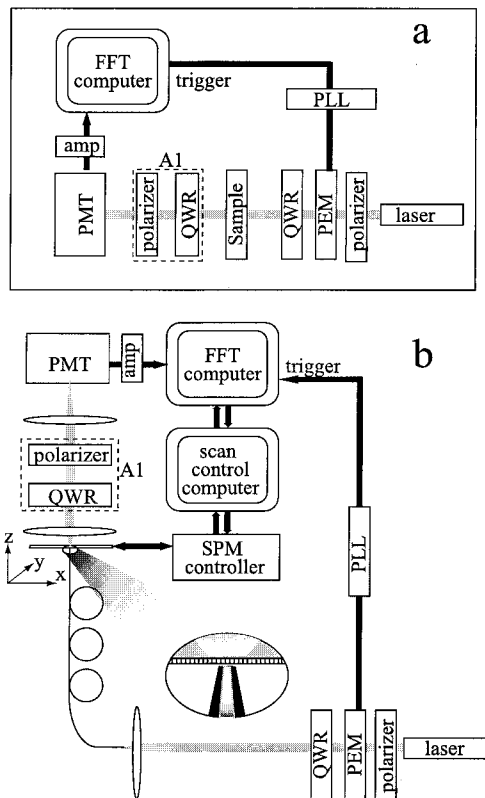


Fig. 1. a, Schematic of a PM polarimeter. Light from a 488 nm laser passes through a polarizer oriented along the x axis. PM light is prepared with a PEM with modulation axis oriented at -45° to x followed by a QWR with a fast axis at -90° . The circular analyzer, A1, is removable. b, Schematic of the apparatus used in this work. PM modulated light is coupled into the cleaved end of the NSOM probe fiber, which passes through a fiber polarization controller ("fiber paddles") used to control the fiber retardance. The tip/sample region is shown in the inset. A timing pulse from the PEM is used via a phase-locked loop to control the data clock (400 kHz). An FFT is performed on the collected time series and the dc, 1ω and 2ω coefficients are extracted at each point in an image scan.

exception rather than the rule, so we make no assumption here about the relative alignments of the eigenvectors of J_r and J_d .

Our instrument is based on a PM polarimetry scheme used by Frattini and Fuller⁴⁶ and Johnson *et al.*⁴⁷ In one implementation (Fig. 1a) light linearly polarized along the x axis is modulated by a photoelastic modulator (PEM) with the modulated axis oriented at -45° . (We use a right-handed coordinate system where the angle is measured from the x axis.) A quarter-wave retarder (QWR) oriented with its fast axis at -90° follows. This combination results in light that is linearly polarized, with a polarization direction that is modulated at frequency $\omega/2\pi$ through an angle d given by the modulation amplitude of the PEM. This light passes through the sample to be collected by a fast detector, typically a photomultiplier tube, PMT. A circular analyzer, A1 (a QWR oriented with its fast axis at 0° followed by a linear polarizer at -45°), may be inserted behind the sample for measurements of retardance. If a

linear retardance is present, the light will have a circular component whose amplitude changes with the input polarization direction. Accordingly, the detected signal after A1 will have harmonics of $\omega/2\pi$. To measure the linear diattenuation, A1 is removed and the intensity of the transmitted light at the detector is measured directly. An overall transmitted intensity that changes with the incident linear polarization direction indicates sample diattenuation, and the magnitude and direction of the diattenuation can be extracted from the periodicity and amplitude of the signal. For example, if we assume that a sample has aligned fast and diattenuating axes, we can calculate the field at the detector (with A1 removed) by using the Jones matrices in Table 1 and the formalism in the Note. Calculating the intensity at the detector from this field, we find that

$$I = \frac{I_0}{2} \{q + r + (q - r)\cos[2\varphi_d - d \sin(\omega t)]\}, \quad (1)$$

where q and r are the transmittances for light polarized parallel and perpendicular, respectively, to the diattenuating axis, φ_d is the alignment angle of the fast and diattenuating axes, d is the modulation depth of the PEM, $\omega/2\pi$ is the modulation frequency, and I_0 is the light intensity incident on the PEM (after the light passes through the first polarizer). Note that, as expected, Eq. (1) shows no dependence on the retardance. With A1 in place the transmitted intensity is a complicated function of both sample retardance and diattenuation. Therefore it is often convenient to limit retardance measurements to systems where diattenuation is negligible. In this case, including the effects of A1 on calculation of the intensity at the detector,

$$I = \frac{I_0}{2} \{1 - \sin(\theta)\sin[2\varphi_b - d \sin(\omega t)]\}, \quad (2)$$

where φ_b is the orientation of the fast axis and θ is the retardance through the material. Equations (1) and (2) represent the approximations most commonly used (in previous work) in the analysis of data taken with this type of PM polarimeter. To reiterate, the approximations and assumptions include (1) alignment of the fast and diattenuating axis for Eq. (1), (2) a purely birefringent sample for Eq. (2), and (3) no circular diattenuation or birefringence in either case. Note that although we use Jones matrices here for simplicity (and since we are not considering depolarization effects), Mueller calculus can also be used and often was used in our data-analysis software.

For analysis purposes Eqs. (1) and (2) are typically expanded into terms proportional to $\sin[d \sin(\omega t)]$ and $\cos[d \sin(\omega t)]$, and these in turn are expanded into Fourier components, yielding

$$\begin{aligned} \cos[d \sin(\omega t)] &= [J_0(d) + 2J_2(d)\cos(2\omega t) + \dots], \\ \sin[d \sin(\omega t)] &= [2J_1(d)\sin(\omega t) + 2J_3(d)\sin(3\omega t) \\ &\quad + \dots]. \end{aligned}$$

As we see below, the first two harmonics contain information needed to determine the linear retardance and diattenuation. With $d = 2.405$, chosen to be the first zero of the zeroth-order Bessel function, Eq. (1) can be written as $I = I_{dc} + I_{1\omega} \sin(\omega t) + I_{2\omega} \cos(2\omega t) + \dots$, where

$$I_{dc} = I_0(q + r)/2, \quad (3)$$

$$I_{1\omega} = I_0(q - r)J_1(d)\sin(2\varphi_d), \quad (4)$$

$$I_{2\omega} = I_0(q - r)J_2(d)\cos(2\varphi_d), \quad (5)$$

where $J_1(d) \cong 0.519$ and $J_2(d) \cong 0.432$. In many experimental strategies,^{30,39,47} two lock-in amplifiers are used to extract the amplitude and phase of $I_{1\omega}$ and $I_{2\omega}$ from the transmitted ac signal, while a low-pass filter is used to obtain I_{dc} . From Eq. (3) and careful measurement of I_0 it is possible to determine $(q + r)$, the sum of the transmittances, although this is not necessary for measurement of the diattenuation, which is the ratio $D \equiv (q - r)/(q + r)$. Instead $I_{1\omega}$ and $I_{2\omega}$ are divided by I_{dc} to obtain

$$R_{1\omega} \equiv I_{1\omega}/I_{dc} = 2DJ_1(d)\sin(2\varphi_d), \quad (6)$$

$$R_{2\omega} \equiv I_{2\omega}/I_{dc} = 2DJ_2(d)\cos(2\varphi_d), \quad (7)$$

from which it is straightforward to solve for D and the angle of the diattenuating axis φ_d .

A similar computation strategy, now applied to the case in which A1 is in place, yields analogous ratios useful for retardance measurements. Equation (2) can also be written in the form $I = I_{dc} + I_{1\omega} \sin(\omega t) + I_{2\omega} \cos(2\omega t) + \dots$, where

$$B_{1\omega} \equiv I_{1\omega}/I_{dc} = 2 \sin(\theta)J_1(d)\sin(2\varphi_b), \quad (8)$$

$$B_{2\omega} \equiv I_{2\omega}/I_{dc} = -2 \sin(\theta)J_2(d)\cos(2\varphi_b). \quad (9)$$

Here θ is the retardance and φ_b is the orientation of the fast axis.

Note that since the 1ω term is always sinusoidal here and the 2ω term cosinusoidal, we generally write an expansion of the detected intensity in the form

$$I(t) = I_0 + I_1 \sin(\omega t) + I_2 \cos(2\omega t) + \dots \quad (10)$$

We use a fast Fourier transform (FFT) of the detected intensity to find the coefficients I_0 , I_1 , and I_2 . These coefficients can be recovered from the FFT by using

$$F(0) = I_0, \quad (11)$$

$$\text{Im}[F(\omega)] = -I_1/2, \quad (12)$$

$$\text{Re}[F(2\omega)] = I_2/2, \quad (13)$$

where $F(\lambda)$ denotes the Fourier transform of $I(t)$ evaluated at the frequency λ . The minus sign preceding the 1ω term and the factor of $1/2$ in the 1ω and 2ω terms arise from the choice of FFT algorithms. These expansions all assume that the phase of the PEM is zero, that is, the retardance of the device is

$d \sin(\omega t)$, not, for example, $d \sin(\omega t + \alpha)$, where α is a fixed phase delay. Generally α is not zero but can be easily measured and accounted for in the data.

The use of a real-time FFT has several advantages over the use of lock-in amplifiers. In addition to it being a more flexible system, permitting extension of the Fourier analysis to more frequency components without adding electronics, this setup permits the use of a single input channel to collect all the polarimetric data. This concern is particularly relevant to the integration of polarimetry with scanning probe microscopy, where each input channel must be synchronized with the position of a scanning stage and the number of input channels is often limited. This design makes it possible to easily incorporate more generalized polarimetry, such as that described by Jellison and Modine,^{50,51} since an arbitrary number of Fourier components can be monitored without the need for further input channels.

3. Near-Field Scanning Optical Microscopy and Instrumentation

Excellent reviews of NSOM have been written by Pohl,⁵² Betzig and Trautman⁵³ and more recently Dunn.⁵⁴ A schematic illustration of our NSOM polarimeter is in Fig. 1b. This system is similar to that used by McDaniel *et al.*³⁹ and more recently by Wei and Fann.³⁰ A polarizer prepares linearly polarized light at 0° . The polarization generator consists of a Hinds Instruments PEM tuned to a nominal modulation frequency of 50 kHz and a modulation axis oriented at -45° . As described above a QWR oriented with its fast axis at -90° follows the PEM. Here a fiber coupler and near-field fiber probe are positioned in front of the sample, and a microscope objective (numerical aperture 0.85) is inserted just after the sample to collect the transmitted light.^{53,54} We use aluminum-coated pulled single-mode fiber probes⁵⁵ with aperture sizes ranging from 80 to 180 nm. The aperture is held 5–10 nm from the sample with a shear-force feedback mechanism⁵⁶ that employs a small piezoelectric tube to sense tip motion. The sample is scanned with a flexure stage (Queensgate), and polarimetric data are acquired at each point in an image. The detector is a PMT and the signal is always reported in this paper as current out of the PMT. To ensure a 1-MHz bandwidth (single pole), the PMT is run at high gain (current output approximately 10 μA with A1 out) and the current amplifier (SRS Model 570) at low gain and high bandwidth (usually 20 $\mu\text{A/V}$). A fast digital I/O board (National Instruments PCI-6110E) is used to acquire polarimetric data; topographic data are acquired with a scanning probe microscope (SPM) control system (RHK SPM 1000 Version 8).

At each pixel in an image, 8192 intensity data points spaced by $\pi/4\omega \cong 2.5 \mu\text{s}$ are acquired. A phase-locked loop is used to lock the sampling frequency to a multiple of the resonant PEM frequency so that the 1ω and 2ω components of the Fourier transform can be easily recovered. That is, the Fourier component representing the positive PEM fre-

quency is commensurate with the 1024th point in our transform, and twice that frequency is commensurate with the 2048th point. Fourier analysis of the intensity versus time signal then yields the amplitude of the dc component and the amplitude and phase (or real and imaginary parts) of the 1ω and 2ω components, which are recorded. The digital I/O board and the SPM software are located on separate computers; hardware handshaking is implemented between the two so that the total system accommodates simultaneous acquisition of all optical and topographic data. Each point in the image takes ≈ 20 ms to acquire; a 128 by 128 image takes a minimum of approximately 6 min to acquire. (The actual image acquisition time in this work was closer to 20 min).

Two important factors, probe diattenuation and probe retardance, must be considered when implementing PM in a near-field microscope. As discussed in detail below, all near-field probes have some diattenuation arising from asymmetries in the probe aperture or tip coating. In addition an improperly coupled fiber will have a diattenuation arising from reflections at the cleaved end.³⁹ This can be sufficiently eliminated by careful coupling into the fiber and use of a high-quality fiber cleaver. Fiber probes also may have linear or circular retardance arising from strain birefringence or geometrical considerations in the fiber tail. The linear retardance can in principle be nulled with a commercially available fiber polarization controller, sometimes called fiber paddles (e.g., see Thorlabs Inc., part FPC030). Although we use this device here, we demonstrate below that the usual method for nulling the fiber retardance in fact fails in the presence of a diattenuating tip. The circular birefringence of the fiber contributes an overall rotation of the incoming polarization, which means that absolute orientations cannot be determined *a priori*. So φ_b and φ_d are measured relative to an arbitrary but fixed axis.³⁹ Fann and Wei³⁰ have recently shown that the tip diattenuation can be measured and accounted for and present a scheme for removing tip diattenuation from a sample diattenuation measurement. Here we extend the analysis and show how residual tip retardance and diattenuation can be both measured and accounted for in the data.

4. Analysis of Probe Diattenuation and Retardance; Nulling the Polarimeter

For a near-field probe the diattenuation and retardance arise from different sources and there is no reason to expect their axes to be aligned. In this work we make the reasonable assumption that retardance arises mainly from strain birefringence and geometrical effects in the fiber, while the diattenuation develops in the tip. For this case we write an expression for the intensity at the detector by considering the following equations. By use of the Jones

calculus, the fields at the input to the fiber (determined by the optics in Fig. 1) are

$$E_0 = \left[R\left(\frac{-\pi}{2}\right) \text{QWR} R^T\left(\frac{-\pi}{2}\right) R\left(\frac{-\pi}{4}\right) \text{PEM} \right. \\ \left. \times R^T\left(\frac{-\pi}{4}\right) \begin{pmatrix} \sqrt{I_0} \\ 0 \end{pmatrix} \right] \\ = \begin{pmatrix} \frac{1}{2} \{1 + \exp[-id \sin(\omega t)]\} \\ \frac{1}{2i} \{1 - \exp[-id \sin(\omega t)]\} \end{pmatrix}$$

(see Table 1 for definitions of the Jones matrices). If circular birefringence is not considered, the expression for the fields at the detector (with A1 and the sample both out) is given by

$$E = R(\varphi_d^t) D(u, v) R^T(\varphi_d^t) R(\varphi_b^t) B(\theta_t) \\ \times R^T(\varphi_b^t) E_0,$$

where the retardance through the fiber is θ_t , the orientation of the fast axis is φ_b^t , the tip diattenuation is $D_t \equiv (u - v)/(u + v)$, and φ_d^t is the diattenuating axis orientation angle. The intensity at the detector is obtained in the usual way from the field. The resulting expressions for the detected intensity contain terms proportional to $\cos[d \sin(\omega t)]$ and $\sin[d \sin(\omega t)]$, as in the example above [Eqs. (1) and (2)]. Fourier expansion of the intensity again yields an equation of the form of Eq. (10), where the components at 1ω and 2ω are given by

$$R_{1\omega}^t \equiv I_{1\omega}/I_{dc} = 2D_t J_1(d) [\sin(2\varphi_b^t) \cos(2\varphi_d^t - 2\varphi_b^t) \\ + \cos(\theta_t) \cos(2\varphi_b^t) \sin(2\varphi_d^t - 2\varphi_b^t)], \quad (14)$$

$$R_{2\omega}^t \equiv I_{2\omega}/I_{dc} = 2D_t J_2(d) [\cos(2\varphi_b^t) \cos(2\varphi_d^t - 2\varphi_b^t) \\ - \cos(\theta_t) \sin(2\varphi_b^t) \sin(2\varphi_d^t - 2\varphi_b^t)]. \quad (15)$$

$J_1(d) \approx 0.519$ and $J_2(d) \approx 0.432$ are the first- and second-order Bessel functions evaluated at the PEM modulation amplitude, $d = 2.405$. Note that both terms are proportional to D_t with factors that depend on both the orientation of the fast and diattenuating axes and the cosine of the probe retardance. As we demonstrate below, if the diattenuation of the tip is not too large, the retardance of the probe can be made small (but not zero) by using the fiber paddles and the fiber-nulling procedure described by McDaniel *et al.*³⁹ To this end we expand these equations for small θ_t (< 0.1) so that $\cos(\theta_t) \approx 1$. The error involved in this approximation will be of the order of θ_t^2 , which for our probes will always be less than 0.01 (see Fig. 6 and Section 5). In this case we can approximate Eqs. (14) and (15) by Eqs. (6) and (7) (i.e., the case of a material with an aligned or zero birefringence):

$$R_{1\omega}^t \approx 2D_t J_1(d) \sin(2\varphi_d^t), \quad (16)$$

$$R_{2\omega}^t \approx 2D_t J_2(d) \cos(2\varphi_d^t). \quad (17)$$

Since both terms are of the order of D_t (which is also small) the accuracy of this measurement depends critically on how well θ_t is nulled. Accordingly, we consider the probe-fiber retardance and discuss in detail the conventional nulling procedure and its deficiencies.

For a linear retardance measurement (A1 in place) of the NSOM probe, the fields at the detector are given by

$$E = R\left(\frac{-\pi}{4}\right) \text{LIN} R^T\left(\frac{-\pi}{4}\right) \text{QWR} R(\varphi_d^t) \\ \times D(u, v) R^T(\varphi_d^t) R(\varphi_b^t) B(\theta_t) R^T(\varphi_b^t) E_0$$

and the intensity ratios are given by

$$B_{1\omega}^t = 2J_1(d) \left[D_t \sin(2\varphi_b^t) \cos(2\varphi_d^t - 2\varphi_b^t) \right. \\ \left. + D_t \cos(\theta_t) \cos(2\varphi_b^t) \sin(2\varphi_d^t - 2\varphi_b^t) \right. \\ \left. + 2 \frac{\sqrt{uv}}{u+v} \sin(\theta_t) \cos(2\varphi_b^t) \right] \\ = R_{1\omega}^t + 2J_1(d) \left[2 \frac{\sqrt{uv}}{u+v} \sin(\theta_t) \cos(2\varphi_b^t) \right], \quad (18)$$

$$B_{2\omega}^t = 2J_2(d) \left[D_t \cos(2\varphi_b^t) \cos(2\varphi_d^t - 2\varphi_b^t) \right. \\ \left. - D_t \cos(\theta_t) \sin(2\varphi_b^t) \sin(2\varphi_d^t - 2\varphi_b^t) \right. \\ \left. - 2 \frac{\sqrt{uv}}{u+v} \sin(\theta_t) \sin(2\varphi_b^t) \right] \\ = R_{2\omega}^t - 2J_2(d) \left[2 \frac{\sqrt{uv}}{u+v} \sin(\theta_t) \sin(2\varphi_b^t) \right], \quad (19)$$

where $B_{1\omega}^t$ is the ratio $I_{1\omega}/I_{dc}$ and $B_{2\omega}^t$ is the ratio $I_{2\omega}/I_{dc}$ for the retardance measurement. Here it is apparent that the diattenuation terms can be accounted for (without approximation) by a simple subtraction of the diattenuation measurement from the retardance measurement. This pattern repeats itself below when we seek to measure the sample retardance in the presence of tip and sample diattenuation.

To null the polarimeter,³⁹ the fiber paddles are adjusted so that $B_{1\omega}^t$ and $B_{2\omega}^t$ are zero (i.e., below the level of noise). Using the approximation for small diattenuation,

$$\frac{\sqrt{uv}}{u+v} = \frac{1}{2} (1 - D_t^2)^{1/2} = \frac{1}{2} \left(1 - \frac{1}{2} D_t^2 + \dots \right) \cong 1/2, \quad (20)$$

we see that Eqs. (18) and (19) can be written as

$$B_{1\omega}^t \cong R_{1\omega}^t + 2J_1(d) \sin(\theta_t) \cos(2\varphi_b^t), \quad (21)$$

$$B_{2\omega}^t \cong R_{2\omega}^t - 2J_2(d) \sin(\theta_t) \sin(2\varphi_b^t). \quad (22)$$

In our measurements we choose tips with diattenuation of ≤ 0.1 . In this case the approximation of Eq. (20) incurs a relative error of less than 0.5%. Setting $B_{1\omega}^t$ and $B_{2\omega}^t$ equal to zero implies that

$$R_{1\omega}^t \cong -2J_1(d) [\sin(\theta_t) \cos(2\varphi_b^t)], \\ R_{2\omega}^t \cong 2J_2(d) [\sin(\theta_t) \sin(2\varphi_b^t)].$$

Using Eqs. (16) and (17) and recalling that $d = 2.405$ [so that $J_1(d) \cong 0.519$ and $J_2(d) \cong 0.432$], we find that $|\sin(\theta_t)| \approx D_t$ and not $\theta_t = 0$. The retardance of the fiber can be nulled to zero only if the diattenuation of the tip is negligible, which it generally is not.

Note that even in the absence of diattenuation both $\theta_t = 0$ and $\theta_t = \pm\pi$ null the polarimeter. This amounts to the addition of a half-wave plate of unknown orientation to our polarimeter scheme. In fact this often turns out to be inconsequential, since the effect of a half-wave plate is to flip the optical axis about the slow axis. Knowledge of the absolute angles is already lost owing to the circular birefringence of the fiber. But in cases in which the tip diattenuation is truly negligible and retardance nulls are therefore accurate, consistent data analysis and accurate relative angular information between images requires that we resolve this ambiguity. This can be done as follows. If we remove the QWR from the input optics and leave A1 in place, we retrieve a 1ω frequency component that is dependent on $\cos(\theta_t)$:

$$I_{1\omega}/I_{dc} = 2J_1(d) \left[2 \frac{\sqrt{uv}}{u+v} \cos(\theta_t) \right. \\ \left. - D_t \sin(\theta_t) \sin(2\varphi_d^t - 2\varphi_b^t) \right]. \quad (23)$$

The 2ω term is identical to Eq. (16) when the QWR is in place. This measurement will be dominated by the first term in the parentheses of Eq. (23), since both D_t and θ_t are small. But the first term is proportional to $\cos(\theta_t)$ and thus will have different signs for $\theta_t = 0$ or $\theta_t = \pm\pi$. This sign change shows up as a phase change (or a change in the sign of the imaginary part) of the Fourier component of the intensity signal at 1ω .

As an illustration of these effects, in Figs. 2a and 2b, we evaluate $B_{1\omega}^t$ and $B_{2\omega}^t$ [by using the full Eqs. (18) and (19)] as a function of θ_t and φ_b^t (400 values of θ_t and 400 values of φ_b^t are used in Fig. 2) for a typical tip with $D_t = 0.0588$, $u = 0.9$, $v = 0.8$, and $\varphi_d^t = 1.3$ rad. Places where $B_{1\omega}^t$ and $B_{2\omega}^t$ are both zero indicate values of θ_t and φ_b^t that result in a polarimeter null. In addition, as discussed above, we can ensure that $\theta_t = 0$ (as opposed to a $\theta_t = \pm\pi$) by removing the QWR and observing the phase of the resulting 1ω component (Fig. 2c). If the phase is $-\pi/2$, the null is correct; if not, the fiber paddles must be repositioned until this condition is met and $B_{1\omega}^t$ and $B_{2\omega}^t$ are again both zero.

In Fig. 3 we examine in more detail the retardance and fast axis alignment for our example tip. For typical experimental conditions the noise in our mea-

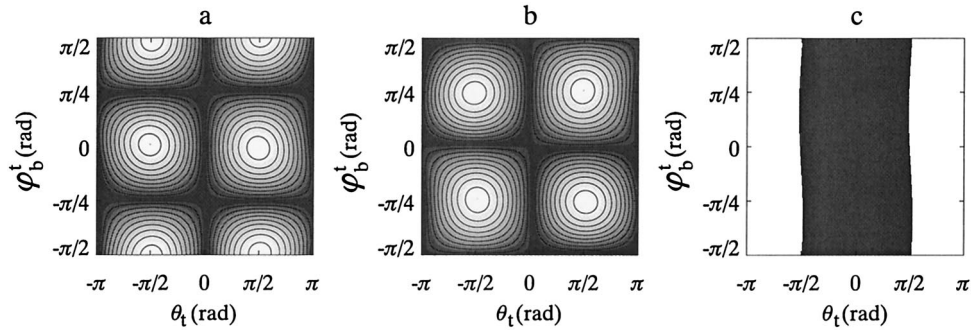


Fig. 2. Nulling the near field polarimeter. Shown in a and b are maps of $B_{1\omega}$ and $B_{2\omega}$ [Eqs. (18) and (19)] respectively, as a function of the probe retardance ($-\pi$ rad to π rad) and fast-axis alignment ($-\pi/2$ rad to $\pi/2$ rad) for a typical tip with the following properties: $D_t = 0.0588$, $x = 0.9$, $y = 0.8$, $\varphi_d^t = 1.3$ rad. Gray scale corresponds to a range of zero (darkest) to 1.04 in a and 0.87 in b. Shown in c is the phase of the 1ω component [Eq. (22)] when the QWR before the fiber in Fig. 1 is removed. A polarimeter “null” is achieved at a simultaneous minimum in a and b and when c is less than zero. In c the gray scale corresponds to the range $-\pi/2$ rad to $\pi/2$ rad with the black areas = $-\pi/2$ rad and the white areas = $\pi/2$ rad.

measurements of $I_{1\omega}$ and $I_{2\omega}$ is always less than 1% of I_0 . In Fig. 3 the retardance is evaluated for points in Figs. 2a and 2b where $B_{1\omega}^t$ and $B_{2\omega}^t$ are less than 0.01 and where Fig. 2c gives a phase of $-\pi/2$. Each of these points represents a candidate null position. Note that at these polarimeter null positions the actual retardance in the fiber probe differs from zero by ± 0.06 rad, depending on the value of φ_b^t . As noted above, nulling the polarimeter in this fashion does not result in zero fiber retardance in the presence of a diattenuating tip.

In our analysis of tip diattenuation we use Eqs. (16) and (17), which do not include terms that are second

order or higher in this small but nonzero retardance. Since our analysis of the retardance also assumes that the diattenuation is small, it is crucial to examine the effect of setting $\theta_t = 0$ in Eqs. (16) and (17). We examine the effect of a nonzero retardance on our diattenuation measurement by using the exact expressions for the diattenuation measurement [Eqs. (14) and (15)] to simulate data on our example tip and then analyze this simulated data by using Eqs. (16) and (17). In Fig. 4 we plot the difference between the exact values for the diattenuation and diattenuating axis and the values that result from the use of

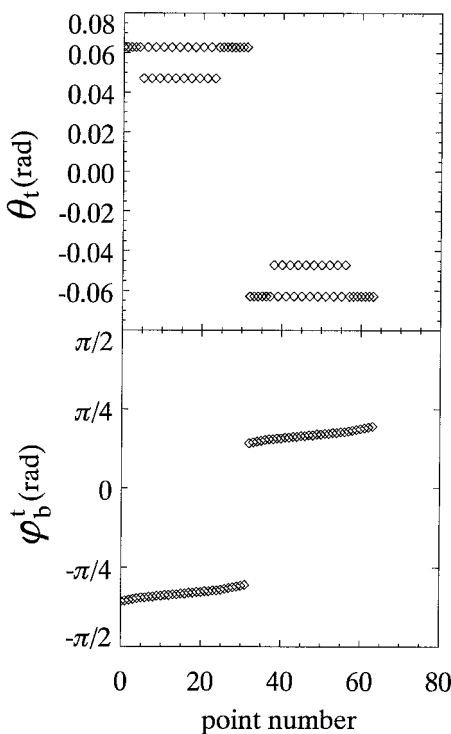


Fig. 3. Plots of (top) the resulting residual probe retardance and (bottom) fast axis alignment for the points in Fig. 2 where a good null is achieved.

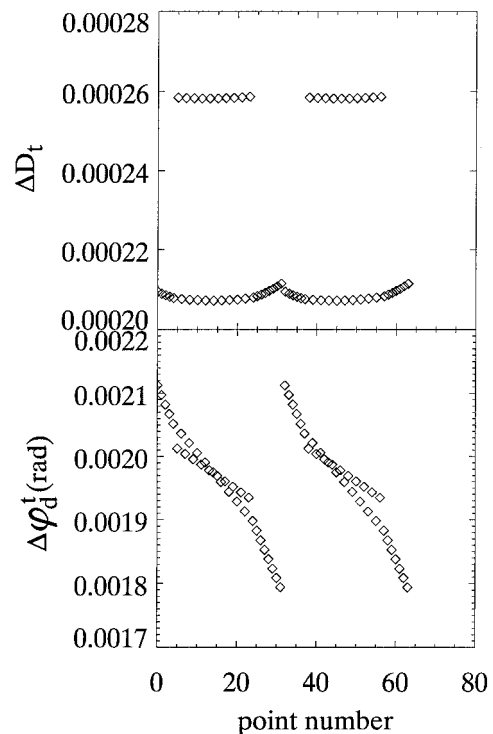


Fig. 4. Plots of the difference between the measured value of D_t and φ_d^t [determined by using Eqs. (16) and (17)] and the actual value used in the model described by Eqs. (14) and (15) for the points in Fig. 2 where a good null is achieved.

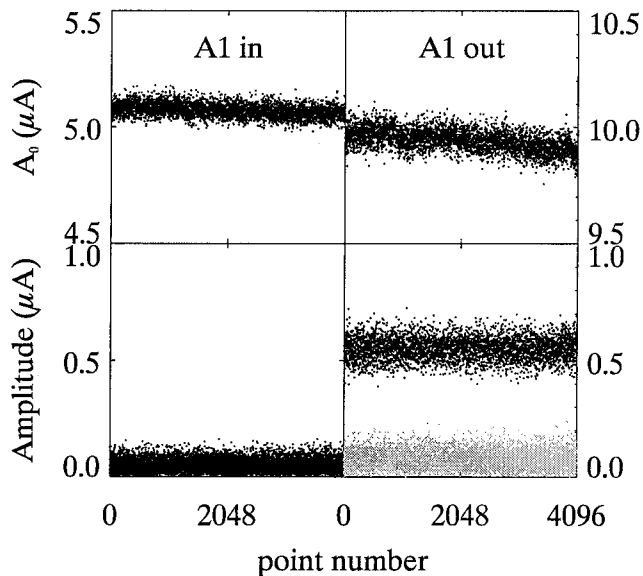


Fig. 5. Amplitudes of the dc (here denoted A_0) 1ω and 2ω Fourier components of the intensity signal measured with A1 in and A1 out collected immediately after nulling the polarimeter. The dc components, plotted in the top panels, in all cases are the largest amplitude component. The 1ω signals are plotted in black, and the 2ω signals are plotted in gray in the bottom panels. Since the polarimeter has been nulled, the 1ω and 2ω components with A1 in place overlap very near zero.

Eqs. (16) and (17) to analyze these data at the various possible null positions. From this analysis it is evident that the range of uncertainty in D_t and φ_d^t is small, less than 1% of the actual D_t and within 0.0022 rad of the actual φ_d^t .

To recapitulate, our polarimeter nulling procedure is similar to that used by McDaniel *et al.*,³⁹ except that we do not assume that this procedure gives us zero NSOM probe retardance. With the sample removed we set up our instrument for a retardance measurement (A1 in place). Fiber paddles are used to zero the 1ω and 2ω signals to within noise levels. We check to see that a $\theta_t = 0$ null has been achieved by removing the QWR and observing the phase of the resulting 1ω component. If this phase is correct, the QWR is replaced and the resulting measurement of $B_{1\omega}^t$ and $B_{2\omega}^t$ is recorded. Next, A1 is removed, $R_{1\omega}^t$ and $R_{2\omega}^t$ are recorded, and the tip diattenuation (D_t and φ_d^t) is measured by using Eqs. (16) and (17). With the diattenuation measurement in hand we calculate the residual probe retardance (θ_t and φ_b^t) by using Eqs. (21) and (22) and $B_{1\omega}^t$, $B_{2\omega}^t$, $R_{1\omega}^t$, and $R_{2\omega}^t$.

5. Measurement of Probe Diattenuation and Retardance

In this section we describe an actual measurement of the NSOM probe polarimetric properties. As discussed above and demonstrated in Sections 6–8, knowledge of the probe properties are necessary for calculation of the sample retardance and diattenuation. Figure 5 illustrates raw polarimetry data collected from an NSOM probe immediately after the

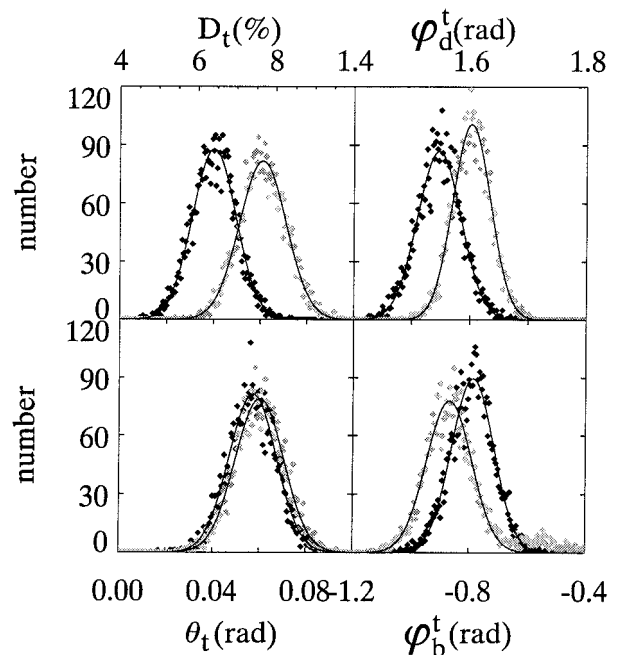


Fig. 6. Histograms of the diattenuation and residual retardance of a near-field probe. Data in black (gray) are taken immediately before (after) the data in Figs. 7–9. This plot illuminates changes in the tip diattenuation and retardance during a scan.

null procedure is performed. (This probe is then used for the measurements in Figs. 8 and 9.) For these tip measurements, data are acquired for 5.5 ms at each of 4096 points over a period of several minutes to measure the tip parameters and their stability. Figure 5 includes plots of the dc, 1ω , and 2ω Fourier component amplitudes for the probe retardance (A1 in) and diattenuation (A1 out) measurements. With A1 out the dc signal is $9.94 \mu\text{A} \pm 0.05 \mu\text{A}$ (standard deviation), the 1ω component is $0.079 \mu\text{A} \pm 0.04 \mu\text{A}$, and the 2ω component is $0.55 \mu\text{A} \pm 0.05 \mu\text{A}$. With A1 in place the dc signal level drops by a factor of 2 ($5.07 \mu\text{A} \pm 0.03 \mu\text{A}$), while the 1ω and 2ω are zeroed at the $0.05 \mu\text{A} \pm 0.03 \mu\text{A}$ value, as expected given the nulling procedure. For these measurements the nominal PMT calibration is $10 \text{ pW}/\mu\text{A}$.

The tip diattenuation is calculated by using the ratios $R_{1\omega}^t$ and $R_{2\omega}^t$, extracted from the data in Fig. 5 (right) and Eqs. (10)–(13), (16), and (17). The resulting distributions of D_t and φ_d^t are shown in the top half of Fig. 6 (by black diamonds). The residual tip retardance is calculated by using the measured ratios $B_{1\omega}^t$, $B_{2\omega}^t$, $R_{1\omega}^t$, and $R_{2\omega}^t$ (which are extracted from the data in Fig. 5). First, the measured ratios $R_{1\omega}^t$ and $R_{2\omega}^t$ at each point are subtracted from the corresponding ratios $B_{1\omega}^t$ and $B_{2\omega}^t$. Approximations (21) and (22) are then used to obtain θ_t and φ_b^t . These distributions are plotted by black diamonds in the lower two panels of Fig. 6.

Several hours after the null was performed and after the images in Figs. 7–9 were acquired, polari-

Table 2. Results of Nonlinear Least-Squares Fits of Data in Fig. 6 to Three-Parameter Gaussian Function Described in the Text

| Distribution | Height, K_0 | Center, K_1 | Width, K_2 |
|--------------------------|---------------|---------------|--------------|
| D_t after null | 87.9 | 0.064 | 0.006 |
| D_t after data | 81.7 | 0.077 | 0.006 |
| φ_d^t after null | 86.8 | 1.55 rad | 0.04 rad |
| φ_d^t after data | 100.7 | 1.60 rad | 0.03 rad |
| θ_t after null | 81.3 | 0.057 rad | 0.010 rad |
| θ_t after data | 79.0 | 0.060 rad | 0.010 rad |
| φ_b^t after null | 89.5 | -0.79 rad | 0.07 rad |
| φ_b^t after data | 77.9 | -0.87 rad | 0.08 rad |

metric data were again collected from this tip. The resulting data are shown as gray diamonds in Fig. 6. The distributions from Fig. 6 were fit to a three-parameter Gaussian, $f = K_0 \exp(-z^2/2)$, $z = (x - K_1)/K_2$, by using a nonlinear least-squares algorithm, to enable statistical comparison. The results are in Table 2. Note that while the retardance is largely unchanged, the diattenuation shifts substantially after the tip is used to collect data. It is commonly reported that aluminum-coated near-field probes change their shape with use and time. Our data demonstrate that such changes significantly affect polarimetric measurements, for when the tip coating is modified, the diattenuation changes. Although the tip retardance was more stable over the data-collection period, note that this is only after a period of significant drift evident after first mounting the probe and most likely due to thermal and physical relaxation of the meter-long fiber tail. Figure 6 illustrates the degree of uncertainty in our polarimetry measurements. The width of these distributions (K_2) is due to the signal-to-noise level of our PMT detector and is therefore dependent on the light throughput of our NSOM probe. The example in Fig. 6 is representative. In general the most severe limitation on our measurements is the shift in probe diattenuation and retardance during the course of data collection. The degree of this shift varied from image scan to image scan. While occasionally it was negligible, generally it was similar to the data in Fig. 6 for the probes in our laboratory. Since these tip data must be used to calculate sample properties, these uncertainties limit the accuracy of our sample diattenuation measurements to roughly the size of the measured tip dichroism shift. Likewise the uncertainty in sample retardance measurements will be limited by shifts in the retardance of the fiber. Since the retardance of the probe drifts less than the diattenuation, and for additional reasons discussed below, the accuracy of retardance measurements is likely to be better than the diattenuation measurements. Overall, as a consequence of these observations, it is recommended that tip diattenuation and retardance be measured both immediately before and immediately after image acquisition. In this study the sample data were analyzed by using both tip measurements as well as their average to gauge the effect of probe changes. Unfortunately gross tip

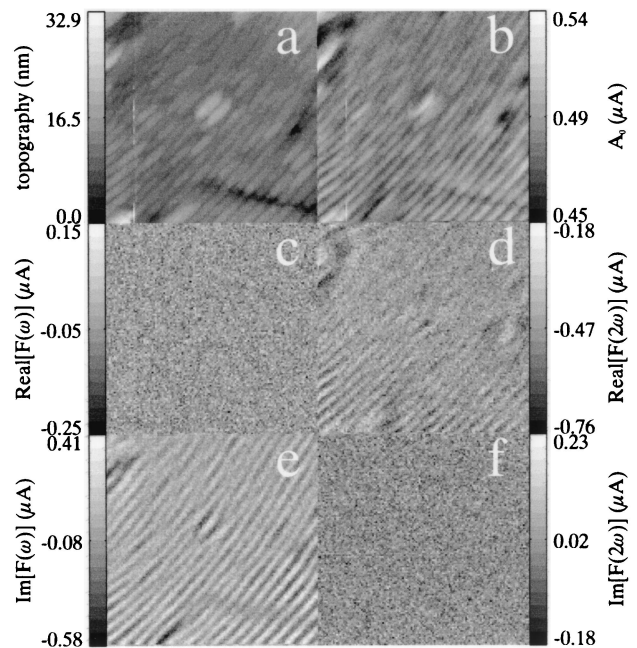


Fig. 7. Raw polarimeter data of a single grain in a block copolymer specimen. Images were acquired simultaneously with A1 out (diattenuation). The micrographs are $4 \mu\text{m} \times 4 \mu\text{m}$ in size: a, topography; b, transmission (dc component of the FFT, here denoted A_0); c, real part of the 1ω component of the FFT; d, real part of the 2ω component of the FFT; e, imaginary part of the 1ω component of the FFT; f, imaginary part of the 2ω component of the FFT.

changes during sample collection can result in data that must be discarded.

6. Analysis of Sample Diattenuation and Retardance

We turn to the subject of sample properties and describe how to account for tip diattenuation and residual retardance in sample polarimetry data. As in the case of tip measurements, there is no assumption that the fast and diattenuating axes of the sample are

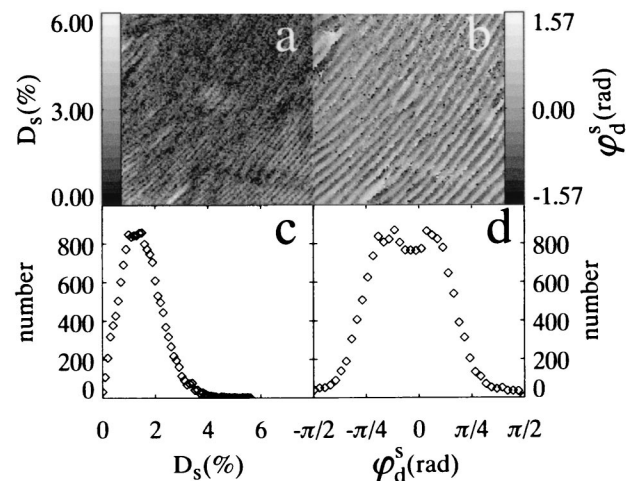


Fig. 8. Diattenuation of the sample in Fig. 7 using the tip data shown as black diamonds in Fig. 6: a, diattenuation; b, diattenuating axis alignment; c, diattenuation histogram; d, histogram of the diattenuating axis alignment angle.

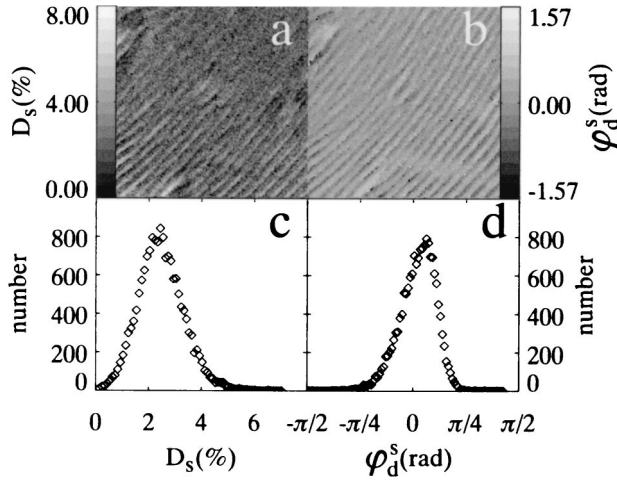


Fig. 9. Diattenuation of the sample in Fig. 7 where the tip data shown as gray diamonds in Fig. 6 are used: a, diattenuation; b, diattenuating axis alignment; c, diattenuation histogram; d, histogram of the diattenuating axis alignment angle.

aligned, and, because of the circular birefringence of the probe, all orientation angles reported are relative.

We begin with the following two assumptions: (1) Our samples are both diattenuating and birefringent but the retardance and diattenuation are small—a reasonable expectation when investigating (as we do in this study) ultrathin polymer films. (2) The tip also exhibits a small diattenuation (<0.1) and retardance (<0.1 rad). For this case, calculation of the full expression for the measured intensity (achieved with Mathematica, Wolfram Research, Inc.) results in a very long expression for $I_{1\omega}$ and $I_{2\omega}$. In lieu of recounting this cumbersome result, we proceed directly to the expressions useful for data analysis. Using the same approximations as above [including Eq. (20) for both tip and sample diattenuation, $\cos(\theta_s) \approx 1$, and $\cos(\theta_t) \approx 1$] and calculation procedures described above, the ratios of the Fourier components are (for the diattenuation measurement, i.e., with A1 removed)

$$R_{1\omega}^s \approx 2J_1(d)[D_t \sin(2\varphi_d^t) + D_s \sin(2\varphi_d^s)], \quad (24)$$

$$R_{2\omega}^s \approx 2J_2(d)[D_t \cos(2\varphi_d^t) + D_s \cos(2\varphi_d^s)]. \quad (25)$$

Note that while the above approximations are correct to first order in θ_s , θ_t , D_t , and D_s , Eqs. (24) and (25) are correct to second order in these parameters and their products. To the same level of approximation, the ratios of the Fourier components for a retardance measurement (A1 in) are

$$B_{1\omega}^s \approx R_{1\omega}^s + 2J_1(d)[\sin(\theta_t)\cos(2\varphi_b^t) + \sin(\theta_s)\cos(2\varphi_b^s)], \quad (26)$$

$$B_{2\omega}^s \approx R_{2\omega}^s - 2J_2(d)[\sin(\theta_t)\sin(2\varphi_b^t) + \sin(\theta_s)\sin(2\varphi_b^s)]. \quad (27)$$

Equations (24) and (25) (and the tip properties) are used to arrive at the sample diattenuation. To de-

termine the sample retardance, we first measure the diattenuation of the sample and then subtract $R_{1\omega}^s$ and $R_{2\omega}^s$ directly from the result of our retardance measurement, as suggested by Eqs. (26) and (27). Note that the tip diattenuation need not be explicitly accounted for in the retardance measurement if this procedure is followed.

7. Example: Measurement of Sample Diattenuation

In this section and Section 8 we present data collected and analyzed with the techniques described above and discuss the experimental uncertainties in these measurements.

Figure 7 shows an example of diattenuation measurements performed on an ultrahigh molecular weight block copolymer specimen.⁴⁰ The microphase separation of block copolymers, caused by the immiscibility of their end-connected constituent polymer chains or blocks, results in a variety of domain motifs tunable through the copolymer composition. A review of these materials and their morphologies is in Ref. 57. These spatial patterns (lamellae, bicontinuous gyroid, hexagonally arranged cylinders, and body-centered cubic spheres) have the potential of exhibiting a photonic band structure with one-, two-, and three-dimensional bandgaps.^{58,59} The large equilibrium periodicity, $L_0 \approx 240$ nm, of microphase separation in our samples makes these materials suitable as self-assembled photonic crystals with stop bands positioned in the visible range.^{42,60} The samples in this study are a polystyrene-*b*-polyisoprene (PS-*b*-PI) block copolymer. Produced by living anionic synthesis in a low-oxygen/low-water environmental chamber, this material has a relative molecular mass, $M_r = 1.2 \times 10^6$, is volume symmetric in composition, and exhibits the lamellar motif with $L_0 \approx 240$ nm. Bulk specimens are processed with a roll-casting technique, which helps order and align the microphase domains.⁶¹ Thin (100-nm) sections are sliced from the bulk by using cryo-ultramicrotomy and deposited onto glass coverslip supports. Subsequent exposure to OsO_4 vapor (2 h) preferentially crosslinks the PI domains. This serves (1) to protect the PI domains from oxygen degradation, (2) to make these domains less compliant and therefore more amenable to our shear-force feedback mechanism, and (3) to enhance the optical contrast between the PS ($n = 1.592$) and PI ($n = 1.53$) domains. Although this staining seems at first glance to be an unfortunate artifact of our technique, note that the increased absorption exhibited by the Os-doped PI domains may mirror absorptive effects inherent in other treatments, e.g., selective domain doping with nanoparticles or chromophores, proposed for enhancing the optical activity of block copolymers and other photonic specimens.

The micrographs in Fig. 7 represent the raw diattenuation data, collected with A1 removed, as described in Sections 2 and 3. All six micrographs were acquired simultaneously. These images center on part of a single grain, showing occasional edge dislocations, and lamellar separations possibly pro-

duced during microtomy. The topography, shown in Fig. 7a, shows a maximum peak-to-valley variation of 33 nm with an rms roughness of 8.0 nm. Figure 7b shows the average transmitted light through the sample (dc amplitude component) measured in microamperes. Nominal calibration of the PMT is 10 pW/ μ A, so the maximum power level in Fig. 7b corresponds to only 5.4 pW. OsO₄ crosslinking of PI causes these domains to contract and enhances their optical absorption. Accordingly the topographically lower domains, which are also more absorbing (darker in Fig. 7b), are identified as PI. However, note that even in the absence of Os staining we expect the PI domains to appear darker compared with PS since the index of refraction of PI is lower.⁶² In Figs. 7c and 7e we show the real and imaginary parts, respectively, of the Fourier component of the intensity signal at frequency ω . In accordance with Eq. (10) we find that the real (cosine) part of this component is zero. Likewise, in Figs. 7d and 7f, which show the real and the imaginary parts of the Fourier component of the intensity signal at frequency 2ω , the imaginary (sine) component is zero, as expected.

Analysis of these data by using Eqs. (24) and (25) and the tip properties in Fig. 6 (measured just before the sample data) yield the sample diattenuation and orientation of the diattenuating axis, as shown in Figs. 8a and 8b, respectively. Image histograms of these properties are shown in Figs. 8c and 8d. Note that the sample diattenuation measured here is small, even when compared with the tip diattenuation, which was near 6% (Fig. 6). Nonetheless a distinct pattern of the diattenuation is observed; it exhibits a maximum at the centers of the PS and PI regions and is minimum near the interface between the domains.

The diattenuation of this sample can be understood by considering the following model, which describes the effects of a near-field aperture on diattenuation measurements. Even for a perfectly symmetric Bethe-Bouwkamp (BB) aperture,^{63–65} the fields confined to the tip aperture are not symmetric. In the BB aperture model the field amplitude shows elongation along the polarization direction. Consider such a field centered over an absorbing PI domain, or stripe, which is similar in width to the aperture size. When the polarization is along the stripe direction, maximum absorption occurs, since the field is aligned and localized along the stripe. When the polarization is perpendicular to the stripe direction, the field is elongated perpendicular to the stripes, a larger portion of the field leaks out over the nonabsorbing PS domain, and more light is transmitted. This anisotropic absorption results in an effective diattenuation with the diattenuating axis oriented perpendicular to the stripe. In this scheme the amplitude of the diattenuation at the center of the stripe depends on the stripe width. For stripes of width approximately equal to or smaller than the tip-aperture diameter, the diattenuation is largest when the tip is centered on the stripe. As the width of the stripe surpasses the aperture in size, the diat-

tenuation is maximum some fixed distance from the edge of the stripe domain and decreases toward zero in the center of the stripe. Over the less-absorbing PS domain the situation is reversed from that described above. For the case where the stripe width is smaller than or approximately equal to the tip-aperture diameter, the diattenuation again reaches a maximum at the center of the domain, but the diattenuating axis would now be aligned parallel to the stripe. This behavior is close to the situation shown in Fig. 8. However, given this hypothesis, it is expected that the difference in diattenuating axis alignment between the PS and the PI domains would be $\pi/2$ rad. From Fig. 8d we see that the distribution of alignment angles has two peaks separated by only 0.8 rad (as determined by a fit to a double Gaussian function). This discrepancy has two likely explanations: (1) The BB theory is not sufficient to describe the tip fields in this experiment, and/or (2) the diattenuation of the tip has not been correctly accounted for. Regarding the first explanation, although BB theory is often sufficient to account for the propagating far fields of an NSOM aperture,⁶⁶ it fails to account for many subtleties of the near or evanescent fields, which depend critically on tip shape and coating.⁶⁷ For an asymmetric aperture or a tip with a rough coating, it is possible that the field asymmetries and therefore the apparent diattenuating axes will be different from those described above. Regarding the second explanation, as noted in Fig. 6 and Section 5, the change in tip diattenuation during a scan is often the largest source of experimental error in these measurements. In Fig. 9 the same data are analyzed by using the tip measurement immediately after taking sample data (Fig. 6, gray diamonds). Here the two peaks in the angular distribution (evident in Fig. 9b) are no longer resolved in the histogram (Fig. 9d). The peak in the diattenuation has also shifted by a factor of almost 2. The overall uncertainty in the diattenuation measurement is roughly determined by the size of the shift in Fig. 6. Note that despite these inaccuracies the precision of this measurement is limited only by the signal to noise of the detector and permits us to resolve small changes between domains, as seen in Figs. 8 and 9.

A more detailed examination of diblock copolymers studied with this technique, in particular a discussion of their retardance and its relationship to their birefringence, can be found in Ref. 40.

8. Example: Measurement of Sample Retardance (and Diattenuation)

To demonstrate retardance measurements, we now turn to a discussion of thin-film PS spherulites. These disklike crystallites consist of radially arranged layers (lamella) of folded chains with intermediate amorphous domains.⁴⁴ Although the structure of bulk polymer spherulites is largely established,^{44,68} a variety of less-understood forms are found in ultrathin (<100-nm) films.^{69–75} The sensitivity and resolution of PM NSOM can illuminate the structure of these two-dimensional crystallites,

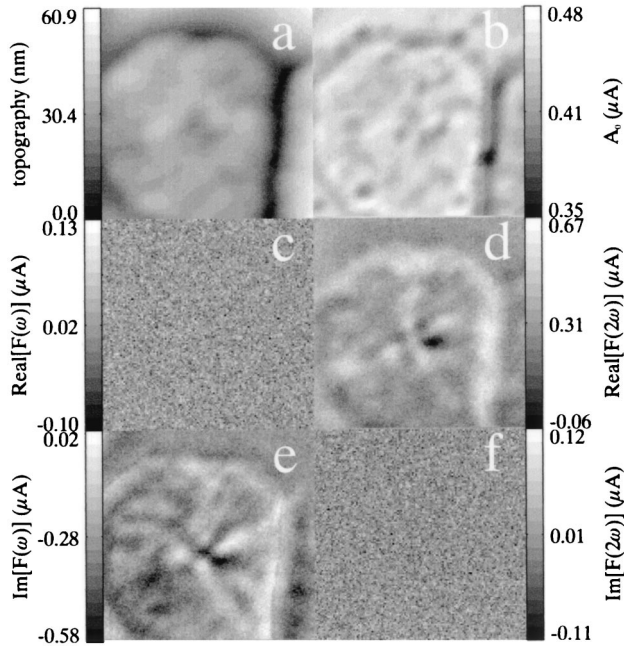


Fig. 10. Raw polarimeter data of a single PS spherulite. Images were acquired simultaneously with A1 out (diattenuation). The micrographs are $4\text{ }\mu\text{m} \times 4\text{ }\mu\text{m}$ in size: a, topography; b, transmission (dc component of the FFT, here denoted A_0); c, real part of the 1ω component of the FFT; d, real part of the 2ω component of the FFT; e, imaginary part of the 1ω component of the FFT; f, imaginary part of the 2ω component of the FFT.

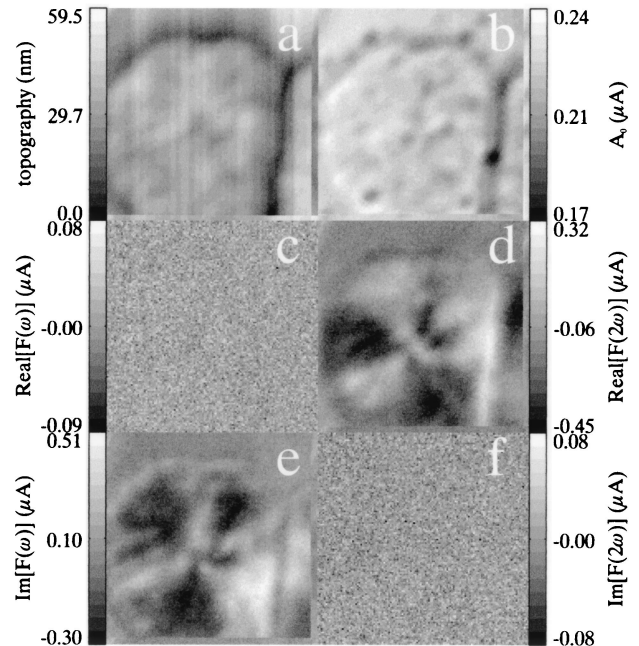


Fig. 11. Raw polarimeter data of a single PS spherulite. Images are acquired simultaneously with A1 in (retardance). The micrographs are $4\text{ }\mu\text{m} \times 4\text{ }\mu\text{m}$ in size: a, topography; b, transmission (dc component of the FFT, here denoted A_0); c, real part of the 1ω component of the FFT; d, real part of the 2ω component of the FFT; e, imaginary part of the 1ω component of the FFT; f, imaginary part of the 2ω component of the FFT.

where traditional techniques may fail because of low resolution and the sparse signal inherent in thin samples.

Spherulite samples were prepared by spin-coating isotactic polystyrene [purchased as a solution of 90% isotactic polystyrene in toluene (mass fraction 4.5%) from Scientific Polymer Products] ($M_r = 6 \times 10^5$, $M_r/M_n = 3.0$) from a 1.0% mass fraction solution in toluene onto glass coverslips. Film thickness was measured to be $85 \pm 4\text{ nm}$ by using an UV-visible reflectance interferometer with a 0.5-mm spot size. Samples were dried under vacuum overnight and crystallized on a gradient hot stage⁷⁶ so that the film temperature spanned 110–130 °C for 2 h. Tapping-mode atomic force microscopy using a Digital Instruments Dimension 3100 Nanoscope III and silicon cantilevers with a spring constant of 30 N/m was used before crystallization to confirm that the film was continuous and contained a low density of defects.

The micrographs in Figs. 10 and 11 represent the raw diattenuation (A1 removed) and retardance (A1 in place) data, respectively, collected from the semi-crystalline PS film specimen, as described in Section 3. Although the six micrographs were acquired simultaneously, two scans over the sample were necessary to obtain the whole data set. These $4\text{ }\mu\text{m} \times 4\text{ }\mu\text{m}$ images show a single spherulite roughly centered in the image and the edge of a second spherulite on the right side. In this specimen, crystal growth was arrested before crystallite impingement was

complete. Accordingly the spherulites are surrounded by amorphous PS. The topography, shown in Fig. 10a (11a), shows a maximum variation of 61 nm (59 nm) with an rms roughness on top of the spherulite of 12 nm (13 nm). Figure 10b (11b) shows the average transmitted light through the sample, measured in microamperes (a raw PMT signal).

Nominal calibration of the PMT for these measurements is 17 pW/μA. In Figs. 10c (11c) and 10e (11e) we show the real and imaginary parts, respectively, of the Fourier component of the intensity signal at frequency 1ω . In accordance with Eq. (10) we find that the real (cosine) part of this component is zero. Likewise in Figs. 10d (11d) and 10f (11f), which show the Fourier components of the intensity signal at frequency 2ω , the imaginary (sine) component is zero, as expected.

These data were analyzed with Eqs. (24)–(27) by using tip-property data collected immediately after the sample measurement was completed. Here the tip had a 4.5% diattenuation and a residual retardance of 0.085 rad. Note again that while the tip diattenuation is needed to obtain diattenuation images of this spherulite, only tip retardance and the raw sample diattenuation data (which include tip diattenuation effects) are needed for the sample retardance measurement [Eqs. (26) and (27)]. In that case the raw diattenuation data are subtracted from the raw retardance data. Figures 12 and 13 show images and histograms of the resulting sample diattenuation and retardance. Although there is no ob-

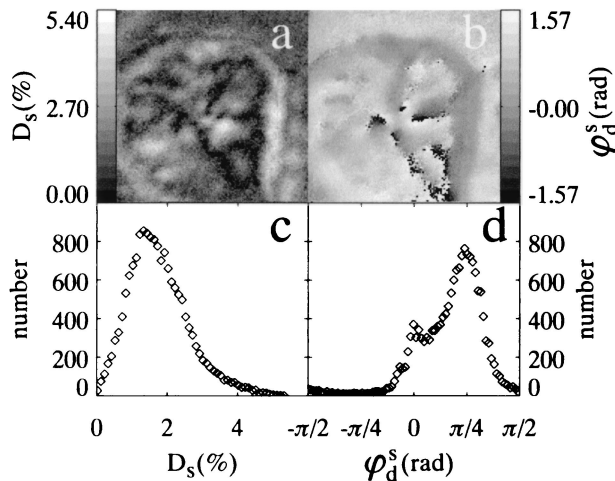


Fig. 12. Diattenuation of the sample in Figs. 10 and 11 calculated with tip data taken immediately after the scans were completed: a, diattenuation; b, diattenuating axis alignment; c, diattenuation histogram; d, histogram of the diattenuating axis alignment angle.

vious mechanism for the apparent diattenuation of these samples, note that topographic features in NSOM can give rise to polarization-dependent transmission⁶² that might account for the diattenuation.

In this case the top portion of these images, which exhibits a band of amorphous material, offers a second method of correcting for background birefringence. The NSOM probe retardance can be estimated by analyzing data in the amorphous region first. We assume that any background retardance in this region is due to the NSOM probe and use this as an alternative measurement of the probe retardance and fast axis alignment. When the data again are analyzed with these new values for the tip parameter, the results in Fig. 14 are obtained. The

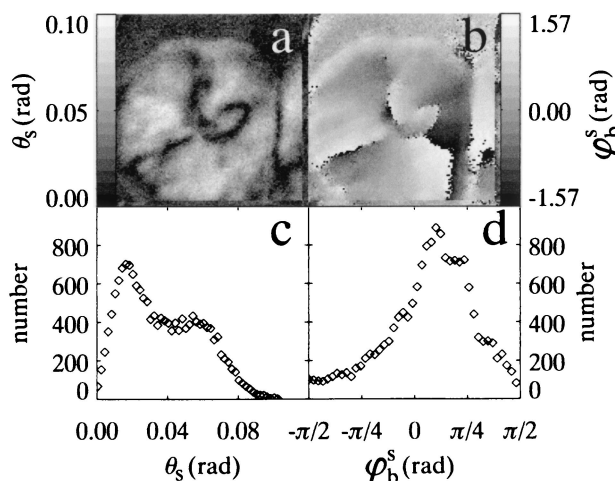


Fig. 13. Retardance of the sample in Figs. 10 and 11 calculated with tip data taken immediately after the scans were completed: a, retardance; b, fast axis alignment; c, retardance histogram showing a clear amorphous peak; d, histogram of the fast axis alignment angle.

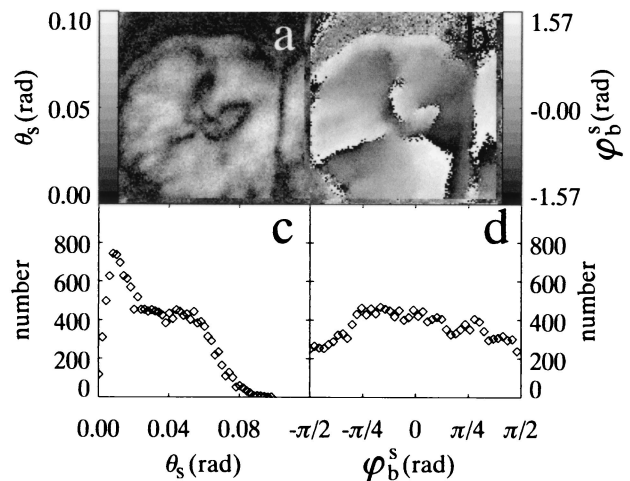


Fig. 14. Retardance of the sample in Figs. 10 and 11 where the amorphous material in the upper central part of the image is used for retardance background subtraction (see text): a, retardance; b, fast axis alignment; c, retardance histogram showing a clear amorphous peak; d, histogram of the fast axis alignment angle.

effects of this new analysis are (1) to shift amorphous regions closer to zero retardance and (2) to modify the fast axis angle histogram so that a uniform distribution of angles results, as might be expected from a spherulitic structure.⁴⁴ In a previous study Campillo and Hsu⁴⁵ performed a similar analysis of background retardance that they attributed to substrate strain. In this work the effect of the tip retardance (which we know to be substantial) is emphasized. A better approximation of the retardance of a birefringent background would probably include contributions from both the tip and the substrate, with separate alignment angles, which would likely add another first-order term to Eqs. (26) and (27).

For both examples of retardance correction, shown in Figs. 13 and 14, the retardance histogram shows two distinct populations, one corresponding to the amorphous region. Inspection of the images reveals that this amorphous material is also intercalated into the spherulite, as expected from these semicrystalline specimens. The radial arrangement of the crystallite lamella is clearly shown in the fast axis image, where, interestingly, defect structures near the crystal nucleus can also be seen. Careful examination of these spherulite structures, whose optical properties can now be mapped in detail with 100-nm resolution by using this technique, will be the subject of future studies.

9. Further Considerations

A. Limitations of Jones and Mueller Formalisms and the Need for Modeling

One serious limitation of this and all previous work concerning near-field polarimetry is the use of a Jones or Mueller formalism, which includes the assumption that light passing through the sample is collimated. The Jones formalism, for example, assumes the existence of a two-dimensional Jones vec-

tor to describe the propagation of light through the polarimeter, which can only be true in the case of a collimated field. In the vicinity of the near-field aperture the field is not collimated and has a significant component polarized along the optical axis of the microscope. Also problematic is the assumption that the intensity distribution is cylindrically symmetric or even plane wave. For example, in Section 7 we show that the apparent diattenuation of our samples is likely not an intrinsic diattenuation but rather a result of the polarization-dependent anisotropy of the near fields and their interaction with the sample. This conclusion cannot be inferred from a Jones-type calculus alone but is supported by preliminary modeling outlined below. Confocal micropolarimetry has a similar drawback. In this case the use of high numerical-aperture (NA) objectives and a pinhole at the detector results in fields that are not collimated at the sample or detector positions. Accordingly a Jones formalism is not applicable. In response to this Török *et al.*⁷⁷ discussed how a generalized (3×3) form of Jones matrices can be used to model the polarization properties of a confocal microscope. A similar treatment applied to NSOM would be difficult or impossible, because there is currently no simple way to model a near-field probe with a generalized Jones matrix, as there is for a high NA lens.

Without these factors included in data analysis, near-field polarimetry data reflect an effective diattenuation and retardance that arise from both the tip-sample interactions and the light-collection scheme. Thus, to measure accurately the intrinsic optical properties of the sample, we need to build a better model that includes both collection optics and near-field effects. In an attempt to address some of these issues we propose the following model, the results of which will be the focus of future work. With the thin-film block copolymer samples as an interesting test case, these specimens are modeled as thin slabs (40–80 nm thick) consisting of alternating parallel stripelike domains (100–200 nm wide) of two different polymers. Three contrast mechanisms are considered: (1) The index of refraction difference between polymer species. (2) The difference in absorption between polymer domains (described qualitatively in relation to Fig. 8). (3) Surface topography that is correlated with the stripe morphology (i.e., one type of domain is higher). The model also includes illumination by a metal-coated optical-fiber NSOM tip and a postsample collection optic with a NA of 1. We use a finite-element time-domain approach to obtain fields transmitted and reflected by the model structured film.⁶² Simulations can be performed for any linear polarization of the probe field in any direction, but here the poignant polarizations are parallel and perpendicular to the stripes. Difference in the far-field transmission for the two polarizations gives the local effective diattenuation. Difference in the far-field phase for the two polarizations gives the local effective retardance.

Each of these three factors can cause an effective

diattenuation or retardance even in the absence of any intrinsic sample diattenuation or birefringence. For the case of absorption contrast, (2) above, in the discussion accompanying Fig. 8 we describe how an effective diattenuation might occur. Regarding index contrast, (1) above, it was recently shown⁶² that a large-index film near an NSOM tip can significantly reduce the tip-air impedance mismatch, leading to a higher light flux from the tip when the probe is over the film. In this case, holes in the film actually transmit less. Such an effect would be expected to persist in the model specimens. However, given the relatively small index changes in these films (for amorphous PS, $n = 1.592$, while for amorphous but crosslinked PI, $n = 1.53$), the effect is small. Because of the anisotropy of the probe fields and the stripe symmetry of the sample, this coupling out of the tip is polarization dependent, which may contribute to effective diattenuation or birefringence. Scattering in the films, the result of local index changes, also contributes to an effective diattenuation or retardance. The third contrast mechanism, topography, may also produce effective diattenuation in films with parallel stripes due to the polarization dependence of diffraction by the topographic grating. Topographic contrast produces an effective diattenuation that is zero near the interfaces and whose diattenuating axis changes direction by 90 deg at the interface, resulting in a pattern of diattenuation similar to that generated by absorption. The effects of topographic and absorption contrast might be distinguishable because the polarization dependence of transmission and reflection has the same sign for absorption contrast and the opposite sign for topographic contrast.

B. Reducing Experimental Uncertainties

Recognizing that diattenuation of the NSOM tip can be problematic, other authors have fabricated more symmetric probes through, for example, ion milling of the aperture.²⁷ However, aluminum-coated apertures can change during data collection. Indeed we find that the largest experimental uncertainties in our NSOM polarimetry data are rooted in changes in tip diattenuation, as illustrated in Fig. 6. Although this problem may be addressed through fabrication of more robust probes,^{37,78–80} a strategy that can be applied to existing probes is to reduce the number of scans necessary to generate polarimetry data, thereby decreasing wear to the tip. In our technique, for example, two images are used to calculate and map the sample retardance. Various schemes exist for reducing the number of required scans. For example, multiple detector channels, each with a different polarization analyzer, can be used simultaneously. In one of the earliest works with a polarimetric setup similar to that employed here,⁴⁷ two channels were used, one with a circular analyzer and one with no analyzer (i.e., one channel for the retardance measurement and one for diattenuation). Alternatively an additional modulator can be included in the postsample optics; here beat-frequency

analysis yields the polarimetric data.^{50,51,81} Since many scanning probe instruments have a limited number of built-in input channels and since NSOM exhibits particularly low signal levels, the latter strategy may prove a better solution. As discussed above Fourier analysis polarimetry facilitates the use of additional modulators since the acquisition of additional Fourier components of the signal is simply a matter of making minor changes to the data-acquisition software.

10. Summary

This work has demonstrated how NSOM polarimetry can be used for quantitative measurements of retardance and diattenuation in the most general sense. First, we demonstrated an application of the Jones matrix formalism to an NSOM polarimeter with several improvements over previous work. In particular we showed how to measure tip diattenuation and residual fiber retardance and properly account for these properties in determination of the diattenuation and retardance of the sample. In contrast to previous work the diattenuating and fast axes need not be aligned in either the sample or NSOM probe. Although our technique relies on the assumption that the sample diattenuation and retardance are small, this approximation is justified in thin specimens. We have shown that when the usual procedure for nulling the polarimeter is performed, tip diattenuation results in a residual retardance. Since this residual retardance is typically comparable in magnitude to the tip diattenuation (and sample properties) it cannot be ignored in polarimetric analysis. Accordingly, the residual retardance must be measured and used in calculating the sample properties. We find that tips with diattenuation of less than 0.1 are suitable for NSOM polarimetry if the analysis procedures described in Sections 4 and 6 are used.

It was shown that measurements of diattenuation and retardance in thin-film samples by use of NSOM contain uncertainties due to changes in the tip diattenuation during scanning, although the drift in retardance with time also contributes to error. A good measurement of the sample properties requires that tip diattenuation and retardance be measured before and after every scan. In addition to providing a means to gauge the noise-limited uncertainty, measurements of tip diattenuation and retardance provide information regarding systematic changes in these properties during the course of data collection. We have also suggested that these errors can be reduced or eliminated by adding an additional collection channel or additional modulator(s) so that all the necessary data can be acquired in a single scan.

We have demonstrated the utility of Fourier analysis for NSOM polarimetry, which permits us to measure many Fourier components of a modulated signal while using only one input channel. Since the number of builtin data-collection channels on many scanning probe instruments is limited, this is a significant improvement over previous efforts. Indeed in prin-

ciple this strategy would allow one to measure all 16 components of the Mueller matrix by using this single channel, as described by Azzam.⁸¹ Although our calculations and models consider pulled-fiber aperture probes, there is no reason that an identical analysis cannot be performed for microfabricated aperture probes,^{37,78–80} so long as their diattenuation is smaller than 0.1.

Finally, we have discussed the limitations of a Jones- or Mueller-matrix approach, which does not handle the confined fields of an NSOM probe correctly. Models to rectify the situation, which were briefly discussed above, will be the subject of future work.

The authors thank and acknowledge P. Connelly, who fabricated the NSOM probes, and T. A. Germer for enlightening discussions. Funding came from the National Institute of Standards (NIST) Advanced Technology Program, NIST director's competence program, the National Research Council (NRC) postdoctoral fellow program. A. Urbas and E. L. Thomas thank the U.S. Air Force Office of Scientific Research (AFOSR) for support through the University of Buffalo Defense-University Research Initiative on Nano Technology (DURINT) grant.

Certain commercial equipment, instruments, or materials are identified to foster understanding. Such identification does not imply recommendation or endorsement by the National Institute of Standards and Technology, or does it imply the materials or equipment identified are necessarily the best available.

References

1. D. W. Pohl, W. Denk, and M. Lanz, "Optical stethoscopy—image recording with resolution $\lambda/20$," *Appl. Phys. Lett.* **44**, 651–653 (1984).
2. E. Betzig, A. Lewis, A. Harootunian, M. Isaacson, and E. Kratschmer, "Near-field scanning optical microscopy (NSOM)—development and biophysical applications," *Biophys. J.* **49**, 269–279 (1986).
3. J. D. Joannopoulos, R. D. Meade, and J. N. Winn, *Photonic Crystals* (Princeton University, Princeton, N.J., 1995).
4. B. Hecht, H. Bielefeldt, Y. Inouye, D. W. Pohl, and L. Novotny, "Facts and artifacts in near-field optical microscopy," *J. Appl. Phys.* **81**, 2492–2498 (1997).
5. G. A. Valaskovic, M. Holton, and G. H. Morrison, "Image contrast of dielectric specimens in transmission mode near-field scanning optical microscopy—imaging properties and tip artifacts," *J. Microsc. (Oxford)* **179**, 29–54 (1995).
6. L. S. Goldner, J. Hwang, G. W. Bryant, M. J. Fasolka, P. P. Absil, J. V. Hryniewicz, F. G. Johnson, H. Shen, and P. T. Ho, "Newton's rings in near-field optics," *Appl. Phys. Lett.* **78**, 583–585 (2001).
7. H. Heinzelmann, B. Hecht, L. Novotny, and D. W. Pohl, "Forbidden light scanning near-field optical microscopy," *J. Microsc. (Oxford)* **177**, 115–118 (1995).
8. L. Novotny, "Allowed and forbidden light in near-field optics. 1. A single dipolar light source," *J. Opt. Soc. Am. A* **14**, 91–104 (1997).
9. L. Novotny, "Allowed and forbidden light in near-field optics. 2. Interacting dipolar particles," *J. Opt. Soc. Am. A* **14**, 105–113 (1997).
10. T. Huser, L. Novotny, T. Lacoste, R. Eckert, and H. Heinzel-

- mann, "Observation and analysis of near-field optical diffraction," *J. Opt. Soc. Am. A* **16**, 141–148 (1999).
11. B. Hecht, H. Bielefeldt, D. W. Pohl, L. Novotny, and H. Heinzelmann, "Influence of detection conditions on near-field optical imaging," *J. Appl. Phys.* **84**, 5873–5882 (1998).
12. E. Betzig, J. K. Trautman, J. S. Weiner, T. D. Harris, and R. Wolfe, "Polarization contrast in near-field scanning optical microscopy," *Appl. Opt.* **31**, 4563–4568 (1992).
13. M. Vaeziravani and R. Toledocrow, "Pure linear-polarization imaging in near-field scanning optical microscopy," *Appl. Phys. Lett.* **63**, 138–140 (1993).
14. R. Toledocrow, J. K. Rogers, F. Seiferth, and M. Vaeziravani, "Contrast mechanisms and imaging modes in near-field optical microscopy," *Ultramicroscopy* **57**, 293–297 (1995).
15. T. J. Silva and S. Schultz, "A scanning near-field optical microscope for the imaging of magnetic domains in reflection," *Rev. Sci. Instrum.* **67**, 715–725 (1996).
16. A. Jalocha and N. F. van Hulst, "Polarization contrast in fluorescence scanning near-field optical reflection microscopy," *J. Opt. Soc. Am. B* **12**, 1577–1580 (1995).
17. D. A. Higgins, P. J. Reid, and P. F. Barbara, "Structure and exciton dynamics in J-aggregates studied by polarization-dependent near-field scanning optical microscopy," *J. Phys. Chem.* **100**, 1174–1180 (1996).
18. J. A. DeAro, K. D. Weston, S. K. Buratto, and U. Lemmer, "Mesoscale optical properties of conjugated polymers probed by near-field scanning optical microscopy," *Chem. Phys. Lett.* **277**, 532–538 (1997).
19. J. A. Teetsov and D. A. Vanden Bout, "Imaging molecular and nanoscale order in conjugated polymer thin films with near-field scanning optical microscopy," *J. Am. Chem. Soc.* **123**, 3605–3606 (2001).
20. J. Teetsov and D. A. Vanden Bout, "Near-field scanning optical microscopy (NSOM) study of alkyl-substituted polyfluorene films: the affect of alkyl substituent length on nanoscale polymer ordering and cluster formation," *Macromol. Symp.* **167**, 153–166 (2001).
21. J. Teetsov and D. A. Vanden Bout, "Near-field scanning optical microscopy studies of nanoscale order in thermally annealed films of poly(9,9-diakylfluorene)," *Langmuir* **18**, 897–903 (2002).
22. D. A. Higgins, X. M. Liao, J. E. Hall, and E. W. Mei, "Simultaneous near-field optical birefringence and fluorescence contrast applied to the study of dye-doped polymer-dispersed liquid crystals," *J. Phys. Chem. B* **105**, 5874–5882 (2001).
23. E. Mei and D. A. Higgins, "Nanometer-scale resolution and depth discrimination in near-field optical microscopy studies of electric-field-induced molecular reorientation dynamics," *J. Chem. Phys.* **112**, 7839–7847 (2000).
24. E. Betzig, J. K. Trautman, R. Wolfe, E. M. Gyorgy, P. L. Finn, M. H. Kryder, and C. H. Chang, "Near-field magnetooptics and high-density data storage," *Appl. Phys. Lett.* **61**, 142–144 (1992).
25. H. Ade, R. ToledoCrow, M. Vaeziravani, and R. J. Spontak, "Observation of polymer birefringence in near-field optical microscopy," *Langmuir* **12**, 231–234 (1996).
26. D. A. Higgins, D. A. VandenBout, J. Kerimo, and P. F. Barbara, "Polarization-modulation near-field scanning optical microscopy of mesostructured materials," *J. Phys. Chem.* **100**, 13794–13803 (1996).
27. T. Lacoste, T. Huser, R. Prioli, and H. Heinzelmann, "Contrast enhancement using polarization-modulation scanning near-field optical microscopy (PM-SNOM)," *Ultramicroscopy* **71**, 333–340 (1998).
28. T. Lacoste, T. Huser, and H. Heinzelmann, "Faraday-rotation imaging by near-field optical microscopy," *Z. Phys. B* **104**, 183–184 (1997).
29. T. Huser, T. Lacoste, H. Heinzelmann, and H. S. Kitzerow, "Scanning near-field optical microscopy of cholesteric liquid crystals," *J. Chem. Phys.* **108**, 7876–7880 (1998).
30. P. K. Wei and W. S. Fann, "The correlation between polarization modulated near-field optical images and the anisotropy of the probe," *J. Microsc. (Oxford)* **202**, 148–153 (2001).
31. C. H. Tan, A. R. Inigo, J. H. Hsu, W. Fann, and P. K. Wei, "Mesoscale structures in luminescent conjugated polymer thin films studied by near-field scanning optical microscopy," *J. Phys. Chem. Solids* **62**, 1643–1654 (2001).
32. P. K. Wei, Y. F. Lin, W. Fann, Y. Z. Lee, and S. A. Chen, "Polarization anisotropy in mesoscale domains of poly(phenylene vinylene) thin films," *Phys. Rev. B* **63**, 045417 (2001).
33. T. J. Silva, S. Schultz, and D. Weller, "Scanning near-field optical microscope for the imaging of magnetic domains in optically opaque materials," *Appl. Phys. Lett.* **65**, 658–660 (1994).
34. V. Kottler, N. Essaidi, N. Ronarch, C. Chappert, and Y. Chen, "Dichroic imaging of magnetic domains with a scanning near-field optical microscope," *J. Magn. Magn. Mater.* **165**, 398–400 (1997).
35. P. Fumagalli, A. Rosenberger, G. Eggers, A. Munnemann, N. Held, and G. Guntherodt, "Quantitative determination of the local Kerr rotation by scanning near-field magneto-optic microscopy," *Appl. Phys. Lett.* **72**, 2803–2805 (1998).
36. O. Bergossi, H. Wioland, S. Hudlet, R. Deturche, and P. Royer, "Near-field magneto-optical circular dichroism using an apertureless probe," *Jpn. J. Appl. Phys. Part 2* **38**, L655–L658 (1999).
37. T. Roder, L. Paelke, N. Held, S. Vinzelberg, and H. S. Kitzerow, "Imaging of liquid crystals using a new scanning near-field optical microscope with microfabricated tips and shear force detection," *Rev. Sci. Instrum.* **71**, 2759–2764 (2000).
38. L. Ramoino, M. Labardi, N. Maghelli, L. Pardi, M. Allegrini, and S. Patane, "Polarization-modulation near-field optical microscope for quantitative local dichroism mapping," *Rev. Sci. Instrum.* **73**, 2051–2056 (2002).
39. E. B. McDaniel, S. C. McClain, and J. W. P. Hsu, "Nanometer scale polarimetry studies using a near-field scanning optical microscope," *Appl. Opt.* **37**, 84–92 (1998).
40. M. J. Fasolka, L. S. Goldner, J. Hwang, A. M. Urbas, P. DeRege, T. Swager, and E. L. Thomas, "Measuring local optical properties: near-field polarimetry of photonic block copolymer morphology," *Phys. Rev. Lett.* **90**, 016107 (2003).
41. A. Urbas, Y. Fink, and E. L. Thomas, "One-dimensionally periodic dielectric reflectors from self-assembled block copolymer-homopolymer blends," *Macromolecules* **32**, 4748–4750 (1999).
42. A. C. Edrington, A. M. Urbas, P. DeRege, C. X. Chen, T. M. Swager, N. Hadjichristidis, M. Xenidou, L. J. Fetters, J. D. Joannopoulos, Y. Fink, and E. L. Thomas, "Polymer-based photonic crystals," *Adv. Mater.* **13**, 421–425 (2001).
43. F. S. Bates and G. H. Fredrickson, "Block copolymer thermodynamics—theory and experiment," *Annu. Rev. Phys. Chem.* **41**, 525–557 (1990).
44. B. Wunderlich, *Macromolecular Physics* (Academic, New York, 1973).
45. A. L. Campillo and J. W. P. Hsu, "Near-field scanning optical microscope studies of the anisotropic stress variations in patterned SiN membranes," *J. Appl. Phys.* **91**, 646–651 (2002).
46. P. L. Frattini and G. G. Fuller, "The dynamics of dilute colloidal suspensions subject to time-dependent flow fields by conservative dichroism," *J. Colloid Interface Sci.* **100**, 506–518 (1984).
47. S. J. Johnson, P. L. Frattini, and G. G. Fuller, "Simultaneous dichroism and birefringence measurements of dilute colloidal suspensions in transient shear flow," *J. Colloid Interface Sci.* **104**, 440–455 (1985).

48. M. Born and E. Wolf, *Principles of Optics*, 4th ed. (Pergamon, New York, 1970), p. 711.
49. S. Y. Lu and R. A. Chipman, "Homogeneous and inhomogeneous Jones matrices," *J. Opt. Soc. Am. A* **11**, 766–773 (1994).
50. G. E. Jellison and F. A. Modine, "Two-modulator generalized ellipsometry: experiment and calibration," *Appl. Opt.* **36**, 8184–8189 (1997).
51. G. E. Jellison and F. A. Modine, "Two-modulator generalized ellipsometry: theory," *Appl. Opt.* **36**, 8190–8198 (1997).
52. D. W. Pohl, "Scanning near-field optical microscopy (SNOM)," *Adv. Opt. Electron Microsc.* **12**, 243–311 (1991).
53. E. Betzig and J. K. Trautman, "Near-field optics—microscopy, spectroscopy, and surface modification beyond the diffraction limit," *Science* **257**, 189–195 (1992).
54. R. C. Dunn, "Near-field scanning optical microscopy," *Chem. Rev.* **99**, 2891–2928 (1999).
55. E. Betzig, J. K. Trautman, T. D. Harris, J. S. Weiner, and R. L. Kostelak, "Breaking the diffraction barrier—optical microscopy on a nanometric scale," *Science* **251**, 1468–1470 (1991).
56. E. Betzig, P. L. Finn, and J. S. Weiner, "Combined shear force and near-field scanning optical microscopy," *Appl. Phys. Lett.* **60**, 2484–2486 (1992).
57. M. J. Fasolka and A. M. Mayes, "Block copolymer thin films: physics and applications," *Annu. Rev. Mater. Res.* **31**, 323–355 (2001).
58. Y. Fink, A. M. Urbas, M. G. Bawendi, J. D. Joannopoulos, and E. L. Thomas, "Block copolymers as photonic bandgap materials," *J. Lightwave Technol.* **17**, 1963–1969 (1999).
59. E. L. Thomas and R. L. Lescanec, "Phase morphology in block-copolymer systems," *Philos. Trans. R. Soc. London Ser. A* **348**, 149–166 (1994).
60. A. Urbas, R. Sharp, Y. Fink, E. L. Thomas, M. Xenidou, and L. J. Fetters, "Tunable block copolymer/homopolymer photonic crystals," *Adv. Mater.* **12**, 812–814 (2000).
61. R. J. Albalak and E. L. Thomas, "Roll-casting of block-copolymers and of block copolymer-homopolymer blends," *J. Polym. Sci. Part B Polym. Phys.* **32**, 341–350 (1994).
62. A. L. Campillo, J. W. P. Hsu, and G. W. Bryant, "Local imaging of photonic structures: image contrast from impedance mismatch," *Opt. Lett.* **27**, 415–417 (2002).
63. H. A. Bethe, "Theory of diffraction by small holes," *Phys. Rev.* **66**, 163–182 (1944).
64. C. J. Bouwkamp, "On the diffraction of electromagnetic waves by small circular disks and holes," *Philips Res. Rep.* **5**, 401–422 (1950).
65. C. J. Bouwkamp, "On Bethe's theory of diffraction by small holes," *Philips Res. Rep.* **5**, 321–332 (1950).
66. G. W. Bryant, E. L. Shirley, L. S. Goldner, E. B. McDaniel, J. W. P. Hsu, and R. J. Tonucci, "Theory of probing a photonic crystal with transmission near-field optical microscopy," *Phys. Rev. B* **58**, 2131–2141 (1998).
67. L. J. Richter, C. E. Jordan, R. R. Cavanagh, G. W. Bryant, A. S. Liu, S. J. Stranick, C. D. Keating, and M. J. Natan, "Influence of secondary tip shape on illumination-mode near-field scanning optical microscopy images," *J. Opt. Soc. Am. A* **16**, 1936–1946 (1999).
68. A. S. Vaughan, "The morphology of semi-crystalline polymers," *Sci. Prog. (London)* **76**, 1–65 (1992).
69. K. Izumi, G. Ping, M. Hashimoto, A. Toda, H. Miyaji, Y. Miyamoto, and Y. Nakagawa, "Crystal growth of polymers in thin films," in *Advances in Understanding of Crystal Growth Mechanisms*, T. Nishinaga, K. Nishioka, J. Harada, A. Sasaki, and H. Takei, eds. (Elsevier Science, Amsterdam, 1997), pp. 337–348.
70. R. L. Jones, S. K. Kumar, D. L. Ho, R. M. Briber, and T. P. Russell, "Chain conformation in ultrathin polymer films using small-angle neutron scattering," *Macromolecules* **34**, 559–567 (2001).
71. O. Mellbring, S. K. Oiseth, A. Krozer, J. Lausmaa, and T. Hjertberg, "Spin coating and characterization of thin high-density polyethylene films," *Macromolecules* **34**, 7496–7503 (2001).
72. G. Reiter, "Mobility of polymers in films thinner than their unperturbed size," *Europhys. Lett.* **23**, 579–584 (1993).
73. G. Reiter and J.-U. Sommer, "Polymer crystallization in quasi-two dimensions. I. Experimental results," *J. Chem. Phys.* **112**, 4376–4383 (2000).
74. Y. Sakai, M. Imai, K. Kaji, and M. Tsuji, "Tip-splitting crystal growth observed in crystallization from thin films of poly(ethylene terephthalate)," *J. Cryst. Growth* **203**, 244–254 (1999).
75. S. Sawamura, H. Miyaji, K. Izumi, S. I. Sutton, and Y. Miyamoto, "Growth rate of isotactic polystyrene crystals in thin films," *J. Phys. Soc. Jpn.* **67**, 3338–3344 (1998).
76. J. C. Meredith, A. P. Smith, A. Karim, and E. J. Amis, "Combinatorial materials science for polymer thin-film dewetting," *Macromolecules* **33**, 9747–9756 (2000).
77. P. Török, P. D. Higdon, and T. Wilson, "On the general properties of polarized light conventional and confocal microscopes," *Opt. Commun.* **148**, 300–315 (1998).
78. W. Noell, M. Abraham, K. Mayr, A. Ruf, J. Barenz, O. Hollricher, O. Marti, and P. Guthner, "Micromachined aperture probe tip for multifunctional scanning probe microscopy," *Appl. Phys. Lett.* **70**, 1236–1238 (1997).
79. S. Werner, O. Rudow, C. Mihalcea, and E. Oesterschulze, "Cantilever probes with aperture tips for polarization-sensitive scanning near-field optical microscopy," *Appl. Phys. A* **66**, S367–S370 (1998).
80. P. N. Minh, T. Ono, S. Tanaka, and M. Esashi, "Spatial distribution and polarization dependence of the optical near-field in a silicon microfabricated probe," *J. Microsc. (Oxford)* **202**, 28–33 (2001).
81. R. M. A. Azzam, "Photopolarimetric measurement of Mueller matrix by Fourier—analysis of a single detected signal," *Opt. Lett.* **2**, 148–150 (1978).